

Accepted Manuscript

Morphological features and associated bottom-current dynamics in the Le Danois Bank region (southern Bay of Biscay, NE Atlantic): A model in a topographically constrained small basin

Shan Liu, David Van Rooij, Thomas Vandorpe, César González-Pola, Gemma Ercilla, Francisco Javier Hernández-Molina

PII: S0967-0637(18)30366-2

DOI: <https://doi.org/10.1016/j.dsr.2019.05.014>

Reference: DSRI 3054

To appear in: *Deep-Sea Research Part I*

Received Date: 20 December 2018

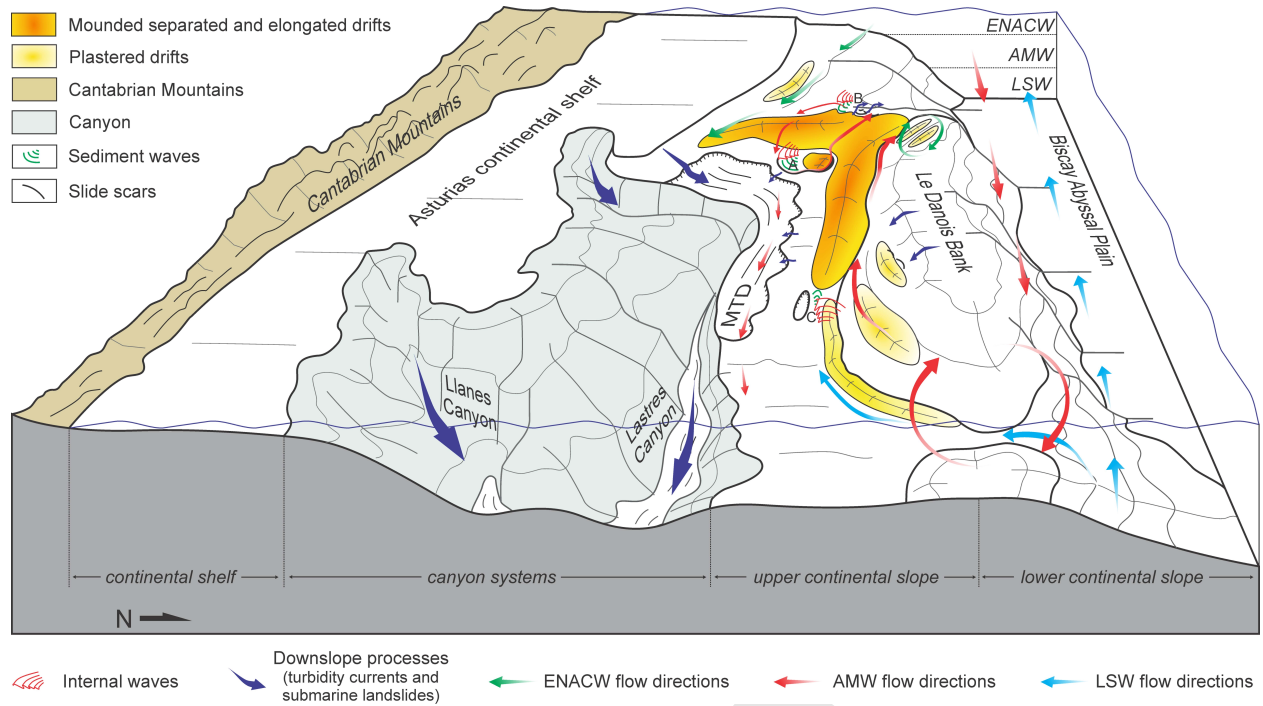
Revised Date: 30 April 2019

Accepted Date: 31 May 2019

Please cite this article as: Liu, S., Van Rooij, D., Vandorpe, T., González-Pola, Cé., Ercilla, G., Hernández-Molina, F.J., Morphological features and associated bottom-current dynamics in the Le Danois Bank region (southern Bay of Biscay, NE Atlantic): A model in a topographically constrained small basin, *Deep-Sea Research Part I* (2019), doi: <https://doi.org/10.1016/j.dsr.2019.05.014>.

This is a PDF file of an unedited manuscript that has been accepted for publication. As a service to our customers we are providing this early version of the manuscript. The manuscript will undergo copyediting, typesetting, and review of the resulting proof before it is published in its final form. Please note that during the production process errors may be discovered which could affect the content, and all legal disclaimers that apply to the journal pertain.





1 **Morphological features and associated bottom-current dynamics in the Le Danois Bank region**
2 **(southern Bay of Biscay, NE Atlantic): a model in a topographically constrained small basin**

3 Shan Liu^{a*}, David Van Rooij^a, Thomas Vandorpe^{a,b}, César González-Pola^c, Gemma Ercilla^d, Francisco Javier
4 Hernández-Molina^e

5
6 ^a *Department of Geology, Ghent University, Campus Sterre (building S8), Krijgslaan 281, B-9000 Gent,*
7 *Belgium*

8 ^b *Flanders Marine Institute (VLIZ), InnovOcean site, Wandelaarkaai 7, 8400 Oostende, Belgium*

9 ^c *Instituto Español de Oceanografía, C.O. Gijón, Avda Príncipe de Asturias 70 bis, E-33212 Gijón, Spain*

10 ^d *Institut de Ciències del Mar, CSIC. Continental Margins Group-GMC. Passeig Marítim de la Barceloneta 37-*
11 *49, 08003, Barcelona, Spain*

12 ^e *Department of Earth Sciences, Royal Holloway University, London, Egham, Surrey TW20 0EX, UK*

13

14 * corresponding author.

15 Tel: + 32 9 264 4591.

16 E-mail address: Shan.Liu@Ugent.Be (S.Liu).

17 Present address: Department of Geology, Ghent University, Campus Sterre (building S8), Krijgslaan 281,
18 B-9000 Gent, Belgium.

19

20 Statement:

21 Declarations of interest: none

22 Colour is not needed for any figures in print

23 **Abstract**

24 The present-day morphology of the Le Danois Bank region has been investigated based on bathymetric
25 and high to ultra-high resolution seismic reflection data. The involved bottom-current processes are
26 associated with the Eastern North Atlantic Central Water, the Atlantic Mediterranean Water and the
27 Labrador Sea Water. Sediments originating from various canyon systems along the Cantabrian Margin and
28 the Asturias continental shelf are transported by downslope and alongslope processes towards the Le
29 Danois intraslope basin. The background flow velocities of bottom currents are all below the threshold (8-
30 10 cm/s) of generating plastered and mounded geometries of contourite drifts. However, bottom currents
31 are locally accelerated (up to 25 cm/s) due to the presence of the Le Danois Bank and the Vizco High,
32 creating a furrow and three moats and generating six plastered drifts, three elongated mounded and
33 separated drifts at different depth intervals. The extension and distribution of the drifts are controlled by
34 slope morphology and/or bottom current velocities. Unlike contourite drifts along other continental
35 slopes, a single contourite drift (the Gijón Drift) with a lateral variation in drift geometry and internal
36 structure indicates the interaction of bottom currents with different flow dynamics. Additionally, scouring
37 of active bottom currents and rapid sedimentation rate of contourite drifts may be at the origin of slope
38 instability events. Besides contourite drifts, internal waves may have induced the formation of sediment
39 waves. In the Le Danois intraslope basin, multiple sedimentary processes work together and shape the
40 present-day seafloor. Bottom currents are focused due to deflection on complex topographical obstacles
41 within a relatively small basin setting, and create a wide variety of sedimentary features, including
42 contourite drifts. The resulting sedimentary features thus have more frequent lateral variations, a feature
43 typical for topographically constrained small basins.

44 **Keywords:** bottom currents; contourites; southern Bay of Biscay; small basin.

45 1 Introduction

46 Bottom currents are currents flowing near the bottom of the ocean (Faugères and Stow, 1993) that can
47 be classified based on their driving forces. Examples are thermohaline circulation, wind-driven currents,
48 geostrophic currents, etc. (Rebesco et al., 2008). Bottom currents generated by thermohaline circulation
49 are described as semi-permanent alongslope currents (Rebesco et al., 2014). Alongslope bottom currents
50 are capable of suspending, transporting and/or controlling the deposition of sediments at the seafloor
51 (Stow et al., 2002). Sediments deposited or significantly affected by bottom currents are known as
52 contourites, and the sedimentary bodies they create are called contourite drifts (Faugères and Stow, 1993;
53 Faugères et al., 1999; Stow et al., 2002). Bottom currents are also capable of creating erosional/non-
54 depositional features such as contourite channels and moats (Rebesco et al., 2014; Hernández-Molina et
55 al., 2016). The lateral and temporal variations of these contourite deposits (drifts) associated with a
56 variety of erosional features lead to the definition of the Contourite Depositional System (CDS)
57 (Hernández-Molina et al., 2008).

58 During the last two decades, numerous studies have focused their attention on large margin-scale
59 contourite deposits, such as the well-studied Cádiz CDS along the SW Iberian continental margin (Llave et
60 al., 2001, 2006; Stow et al., 2013), the Lofoten and Vesterålen Drifts along the NW European Atlantic
61 margin (Laberg et al., 2005; Stoker et al., 2005) and the giant CDS along the Argentine continental margin
62 (Preu et al., 2012, 2013). Bottom-current processes associated with these large-scale drift systems are
63 being widely investigated (Maldonado et al., 2005; Hernández-Molina et al., 2010). However, small-scale
64 bottom-currents in smaller basins and around topographical obstacles could strongly interact with
65 seafloor morphology and oceanographic processes (e.g. internal waves/tides, eddies, Chen et al., 2019).
66 The related processes received far less attention and their mechanisms are not yet fully understood
67 (Turnewitsch et al., 2004; Rebesco et al., 2014; Van Rooij et al., 2016; Zhang et al., 2016).

68 Small-scale contourite drifts have been documented at different continental margins (Tournadour et al.,
69 2015; Juan et al., 2016). They are reported around the mud volcanoes of the Moroccan Atlantic margin
70 (Vandorpe et al., 2016) and the Gulf of Cádiz (Palomino et al., 2016), around the Pontevedra obstacle in
71 the Galicia Bank region (Ercilla et al., 2011; Zhang et al., 2016), associated with cold-water coral mounds
72 in the Porcupine Seabight, SW of Ireland (Van Rooij et al., 2007), around a seamount in the South China

73 Sea (Chen, et al., 2014) and associated with the Le Danois Bank along the northern Iberian continental
74 margin (Van Rooij et al., 2010). Whereas the steep northern flank of the Le Danois Bank is dominated by
75 gravitational processes, the intraslope basin hosts small-scale contourite deposits. The related drift
76 systems extend from the Le Danois Bank (in the north) to the Asturias continental upper slope (in the
77 south) and are dominating the geomorphology of the present intraslope basin. Based on some sparsely
78 distributed seismic profiles, these drift systems seem to be highly affected by the interaction between the
79 intermediate water mass and the associated morphologies of the intraslope basin (Ercilla et al., 2008;
80 Iglesias, 2009; Van Rooij et al., 2010). Types and dimensions of depositional, erosional and mixed features
81 show remarkable variations: elongated mounded and separated drifts (the Le Danois and the Gijón Drifts),
82 plastered drifts, moats (the Le Danois and the Gijón Moats) and slide scars have all been identified
83 (Iglesias, 2009; Van Rooij et al., 2010). However, the dynamic interaction between the present-day
84 bottom-current circulation and the detailed characteristics, as well as the spatial variability of the drift
85 systems are still not fully understood.

86 Due to the presence of a topographic obstacle (e.g. a coral bank, slide scar or fault), bottom currents will
87 enhance locally and have the capability of creating flow filaments, in turn creating their own erosional and
88 depositional features (Stow et al., 2002, 2008; Rebesco et al., 2008, 2014). The Le Danois Bank region is
89 ideal for investigating the relationship between various topographic obstacles, bottom current dynamics,
90 and different contourite features. Mediterranean Outflow Water (MOW) is considered to be the most
91 important water mass (Ercilla et al., 2008, 2011; Van Rooij et al., 2010), referring to the pure thermohaline
92 outflow in the Gulf of Cádiz (Hernández-Molina et al., 2014). This water mass will now be referred to as
93 the Atlantic Mediterranean Water (AMW), due to its different physical properties and dynamics (Rogerson
94 et al., 2012; Flecker et al., 2015). The location of the Le Danois Bank region is thus key for better
95 understanding the local interaction of the AMW with the continental slope sedimentary processes.

96 This study aims to provide a comprehensive description of the distribution and current morphology of
97 various depositional and erosional features of the Le Danois Bank region. By combining previous
98 observations with additional ones derived from more recent seismic datasets and improved insights
99 regarding the present-day oceanographic setting, this study aims to improve the understanding of the
100 recent interaction between topographic obstacles and bottom currents. As such, this study introduces a

101 unique model related to the responsible bottom-current dynamics in a topographically constrained small
102 basin.

103 **2 Regional setting**

104 2.1 Geology and morphology

105 The Le Danois Bank, an E-W narrow topographic high, is located at the Cantabrian continental slope, in
106 the southern Bay of Biscay (Fig. 1). The northern flank (mean slope values between 18° and 20°, reaching
107 34° locally) of the Le Danois Bank steeply drops into the Biscay abyssal plain, whereas the southern flank
108 (slope gradient varying from 0.8° to 15°) is connected to the upper continental slope (Figs. 2, 3). The
109 presence of the Le Danois Bank creates an intraslope basin (about 65 km long and 15-25 km wide)
110 between the bank and the Asturias continental shelf (Figs. 2, 3). This basin is bounded to the west by the
111 Vizco High and to the southeast by the Lastres Canyon (Fig. 1b). The basin becomes shallower from the
112 centre (1070 m) towards the bank (855 m) and the continental shelf (443 m).

113 The Cantabrian margin was deformed by compression during the Early Paleocene to the Eocene when
114 the northward displacement of the African plate led to the Iberian-European collision, resulting in the
115 Cantabrian-Pyrenean chain along the northern border of the Iberian plate (Boillot et al., 1979; Alvarez-
116 Marrón et al., 1996). In the Early Oligocene, the subduction of the Iberian plate beneath the European
117 plate, as well as shortening of the northern Iberia plate, resulted in regional compression in the Bay of
118 Biscay (Fernández-Lozano et al., 2011). The subsequent mantle exhumation and crustal thinning beneath
119 the Cantabrian continental margin induced the formation of the Le Danois Bank and the intraslope basin
120 (Vissers and Meijer, 2012; Cadenas and Fernandez-Viejo, 2016). At the end of the Oligocene, the collision
121 of the Iberian and European plates halted and there is no evidence of large-scale tectonic activity in the Le
122 Danois Bank region from the Miocene onwards (Muñoz, 2002; Vergés et al., 2002; Roca et al., 2011;
123 Tugend et al., 2014; Cadenas and Fernandez-Viejo, 2016).

124 The contourite deposits (drifts) are observed in the Pliocene unit (Van Rooij et al., 2010). Confined
125 contourite drifts have been identified in the Upper Pliocene unit and the elongated mounded and
126 separated drifts are generated in the Middle Pleistocene unit (Van Rooij et al., 2010). The sediment supply
127 consists of fine-grained material eroded from the Cantabrian Mountain range (Gaudin et al., 2006; Ercilla

128 et al., 2008). Gómez-Ballesteros et al. (2014) suggested that the sediments are transported into the ocean
129 through the Narcea and Nalón rivers (Fig. 1a) and move along the Cantabrian continental slope eastwards
130 by means of alongslope currents.

131 2.2 Oceanography

132 At present, three water masses are found below the surface mixed layer in the Le Danois Bank region: (1)
133 The Eastern North Atlantic Central Water (ENACW) between 350 and 600 m water depth (McCartney and
134 Mauritzen, 2001), (2) the Atlantic Mediterranean Water (AMW) between 750 and 1550 m water depth
135 (Iorga and Lozier, 1999a, b), and (3) the Labrador Sea Water (LSW) between 1750 and 2000 m water
136 depth (van Aken, 2000a). Between these water masses, two interfaces are located respectively at 600 to
137 750 m and 1550 to 1750 m water depth (van Aken, 2000a, b) (Fig. 4).

138 The ENACW originates at the northeast of the Azores (Pollard et al., 1996). Subtropical origin ENACW
139 enters the Bay of Biscay as an eastward slope current along the northern Iberian continental slope
140 (Pingree, 1993; Pollard et al., 1996; McCartney and Mauritzen, 2001). Its subtropical branch constitutes an
141 eastward slope current along the northern Iberian continental slope and flows polewards (Pingree and Le
142 Cann, 1990; van Aken, 2000b). The ENACW contains relatively small variations in temperature and
143 salinity in the Bay of Biscay, ranging respectively between 11.8° to 12.2 °C and 35.53 to 35.58 (Haynes and
144 Barton, 1990; Ríos et al., 1992; Pingree, 1993). The mean velocity is around 1 cm/s in the southern Bay of
145 Biscay (Frouin et al., 1990; Lavín et al., 2006). In the Le Danois Bank region, the ENACW has a higher
146 velocity (10-30 cm/s) and flows eastwards along the Asturias continental upper slope (Lavín et al., 2006;
147 González-Pola et al., 2012). Along the rim of the eastern summit of the Le Danois Bank, an anticyclonic
148 circulation with a velocity of about 15 cm/s has been observed at the ENACW depth range (González-Pola
149 et al., 2012) (Fig. 1b). This circulation cell is most likely induced by a steady background flow impinging
150 on the topographical barrier or interaction between periodically enhanced currents and the Le Danois
151 Bank (González-Pola et al., 2012). Its core is located at 400 m water depth with a minimum salinity of 35.5
152 (Fig. 4).

153 At a depth of about 1000 m, a core of eastward-flowing AMW is observed hugging the northern Iberian
154 continental slope with a mean velocity of 1-5 cm/s (Iorga and Lozier, 1999a). In the Le Danois Bank region,
155 its maximum salinity reaches 35.8 while the temperature remains about 10°C (Fig. 4b). Most of the AMW

156 flow penetrates along the northern flank of the Le Danois Bank and there is no dominant flow within the
157 intraslope basin at present day (González-Pola, data not shown). The intraslope basin has the capability to
158 develop its own recirculation pattern, due to the topographic constraints of the Le Danois Bank and the
159 continental shelf (González-Pola et al., 2012). Anticyclonic recirculation during upwelling conditions and
160 cyclonic recirculation during downwelling conditions have been observed at the AMW level between the
161 bank and the continental shelf (González-Pola, personal communication) (Fig. 1b). At the eastern edge of
162 the Le Danois Bank, a pronounced anticyclonic circulation, potentially caused by eddy shedding from the
163 shelf, is also recorded at the AMW level by a single observation (González-Pola et al., 2012) (Fig. 1b). It
164 symmetrically distributes over the bank and has a mean velocity of 10 cm/s (González-Pola et al., 2012).

165 Below the AMW, the LSW penetrates along the northern Iberian continental margin from east to west
166 (Lazier, 1973; Gascard and Clarke, 1983; van Aken, 2000a). In the study area, the core of the LSW is
167 recognized at 1800 m water depth with a minimum salinity of 35.05 (Figs. 4b, f). Due to the depth of the
168 intraslope basin (max. 1720 m), the LSW is hindered and fails to penetrate the basin towards the west.
169 Intense diapycnal mixing, resulting from the highly energetic internal tidal waves, has been observed
170 between the LSW and the AMW over the Cantabrian continental slope (Pingree, 1993; van Aken, 2000a, b).
171 This mixing action makes the Le Danois Bank region a focal point for the occurrence of the high-energetic
172 turbulent events at the interface between the AMW and the LSW (van Aken, 2000b; Lavín et al., 2006).

173 **3 Material and methods**

174 Three sets of reflection seismic data have been used for this study (Fig. 1b). These datasets embrace
175 different vertical resolutions, ranging from high to ultra-high. These different datasets contain nearly
176 overlapping NNE-SSW to N-S orientated profiles, enabling a more detailed seismic interpretation of the
177 morphological features. The ultra-high resolution TOPAS (topographic parametric sonar) PS18 profiles
178 were obtained during the BIO Hespérides campaign MARCONI II in 2003 (Ercilla et al., 2008; Iglesias,
179 2009) and penetrates down to 200 ms two-way travel time (TWT) at full oceanic depth. The primary
180 frequency was 15 kHz (secondary 0.5-6 kHz), while the maximum vertical resolution was about 0.2 m.
181 Four S-N trending and three E-W trending TOPAS lines were acquired in the study area with a mean
182 spacing of 25 km. The high-resolution single-channel sparker seismic profiles were obtained during the
183 R/V Belgica cruise ST1118a in June 2011. A 500 J energy SIG sparker (800 Hz frequency) has been used,

184 with a shot interval of 2.5 s. The penetration depth of the acoustic signal varies around 500 ms TWT and
185 the vertical resolution varies around 1.5 m. Twelve NNE-SSW and fifteen W-E to WNW-ESE orientated
186 sparker seismic lines with a spacing of 3-5 km have been acquired. The three-channel airgun seismic
187 records have been acquired during the MARCONI II campaign. The seismic source, a 5-meter-long airgun
188 array of 6 Sercel G-GUN II (140 bars, 80 Hz frequency), was located at 2.5 m depth with a shot interval of 6
189 s. The receiver system was a 150 m SIG streamer with 3 sections of 40 hydrophones each. The penetration
190 of the acoustic signal is about 1.5 s TWT. The standard vertical resolution was about 4.5 m. Seventeen
191 NNE-SSW and nine WNW-ESE orientated airgun seismic lines with a spacing of 10-15 km were surveyed.

192 The TOPAS and sparker seismic data have been processed using the DECO Geophysical RadexPro
193 Software. They were corrected for spherical divergence, amplitude loss and burst noise. The sparker
194 seismic data was further processed using a swell filter and an Ormsby bandpass filter (160 to 250 Hz and
195 1400 to 1500 Hz). The airgun seismic data was processed on board using the Delph Seismic Plus Software
196 and included a bandpass filter (2.5 kHz high pass and 80 kHz low pass). Afterwards, the data were
197 processed by applying a spherical divergence correction, an interactive velocity analysis, and a burst noise
198 removal.

199 The multibeam data had been acquired with the RV Vizconde de Eza in 2003 within the framework of
200 the ECOMARG project (<http://www.ecomarg.com/>). The positioning data was provided by Seapath 204,
201 while the SIMRAD EM 300 provided the bathymetric data. This system operated at a water depth ranging
202 between 200 and 3000 m and had a vertical error of less than 1 %. The sampling frequency was set at 30
203 kHz. The footprint is 15 x 15 m at 500-600 m and 25 x 25 m at about 1000 m. The data covered an area of
204 5530 km². It encompasses the entire study area including the Le Danois Bank, the intraslope basin, the
205 Vizco High, the Lastres Canyon and the adjacent continental shelf (Figs. 2, 3). Vertical CTD profiles were
206 extracted from the World Ocean Database (2013) (<https://www.nodc.noaa.gov/OC5/WOD13/>). The
207 salinity and temperature cross sections (Figs. 4, 9) were made using Ocean Data View (ODV) software.

208 **4 Results**

209 In the Le Danois Bank region, the most pronounced physiographic features were already reported by
210 Ercilla et al. (2008) and Van Rooij et al. (2010). Based on these previous results, the combination of three
211 currently available seismic datasets, the multibeam data and the updated classification of contourite drifts

212 presented in Rebesco et al. (2014), new insights have been provided on morphosedimentary
213 characteristics of alongslope, downslope and mixed features and their distribution.

214 4.1 Alongslope features

215 4.1.1 Elongated mounded and separated drifts

216 The SW-NE oriented Le Danois Drift is located between 790 and 1080 m water depth (Figs. 5, 6a, b, c).
217 The drift encompasses an area of 242 km² and is about 42 km long and 4-11 km wide and 50 m high. The
218 main element characterizing this drift is the high mounded geometry (slope gradient of 0.5° to 2.8°) (Fig.
219 3). Internally, it comprises continuous parallel-stratified reflections, onlapping upslope with a sigmoidal-
220 oblique progradational pattern towards the Le Danois Bank (Fig. 6c). Towards the south, the mean
221 thickness laterally decreases from 280 to 130 ms TWT. At the western limit of the Le Danois Drift, the
222 thickness reaches its minimum (10-20 ms TWT).

223 The NW-SE oriented Gijón Drift is located at the southernmost part of the intraslope basin between 320
224 m and 1060 m water depth (Figs. 5, 6a, b, d). The drift is 34 km long and 2 to 13 km wide. It displays a
225 broad mounded geometry (slope gradient of 1° to 3°) and a basal unconformity with onlap terminations
226 (Fig. 6d). The mounded part rises 80 m above the surrounding seafloor. The seismic facies of the Gijón
227 Drift is characterized by stratified layers of continuous sigmoidal reflections interbedded with
228 discontinuous low-amplitude chaotic reflections (Figs. 6a, d). Towards the north, the sedimentary bodies
229 of the Gijón and the Le Danois Drifts overlapped, where the seismic reflections are continuous parallel-
230 even configurations (Fig. 6a). The thickness of the Gijón Drift gradually decreases from 320 to 30 ms TWT
231 towards the southeast. The southeast extension of the Gijón Drift is limited by the presence of the Lastres
232 Canyon (Fig. 5). Towards the northwest, the geometry of the Gijón Drift evolves from elongated and
233 mounded (Figs. 6a, d) to confined and mounded (Fig. 6b). The change of the geometry is associated with a
234 reduction in thickness (from 220 to 110 ms TWT). The internal structure of this part of the Gijón Drift is
235 characterized by convex-upward seismic patterns with high- to medium-amplitude sigmoidal reflections
236 thinning towards the edges (Fig. 6b).

237 At the centre of the intraslope basin, a small elongated mounded and separated drift is identified (Fig.
238 6c). Based on the proximal physiographic feature, the Asturias continental shelf, this drift is referred to as

239 the Asturias Drift (Fig. 5). The Asturias Drift covers an area of 21 km² at water depths between 900 and
240 1080 m. It is characterized by an unconformity surface with onlap and downlap terminations and
241 mounded geometry (slope gradient of about 1°) (Figs. 3, 6c). The drift displays a sigmoidal-oblique
242 seismic stacking pattern (Fig. 6c). The maximum thickness is 90 ms TWT, decreasing towards the
243 southwest.

244 4.1.2 Plastered drifts

245 Along the upper continental slope, WNW-ESE trending plastered drift 1 is identified between 200 and
246 500 m. It encompasses an area of about 48 km² and has a length of about 7.5 km and a width of 1.5-2.5 km
247 (Figs. 3, 5, 6d). The drifts are characterized by sigmoidal reflections draped over the upper continental
248 slope and is about 10 to 90 ms TWT thick. At the southern flank of the Le Danois Bank, four E-W trending
249 narrow plastered drifts are recognized at different water depths. Plastered drifts 2 (9 km long and 2.4 km
250 wide, from 528 to 642 m) and 3 (9.3 km long and 0.8 km wide, from 715 to 782 m) are located at the
251 western edge of the Le Danois Bank and are separated by a ridge (Figs. 5, 7a). The ridge (10 km long, 600
252 m wide) rises 20 m above the surrounding seafloor with a WNW-ESE orientation. Plastered drift 4 (from
253 870 to 1100 m) is positioned at the upper southeast flank of the bank and has a length of 10 km and a
254 width of 0.8 to 1.1 km (Figs. 3, 7b, c). Plastered drift 5 (from 1350 to 1780 m), located at the lower
255 southeast flank of the bank, is 7 km long and 1.8-3.9 km wide (Figs. 3, 5, 7d). Along the southeast foot of
256 the Le Danois Bank, the SW-NE oriented plastered drift 6 is located at water depths between 1760 and
257 1920 m (Figs. 3, 5, 7e). This plastered drift covers an area of 56 km² and is about 18 km long and 1.8 km
258 wide. The thickness ranges from 20 to 60 ms TWT. The internal structure is characterized by sigmoid
259 reflection configurations and an unconformity surface with onlap and downlap terminations.

260 4.1.3 Moats and furrows

261 The Le Danois Moat parallels the southern foot of the Le Danois Bank between 866 and 1530 m water
262 depth (Figs. 6a, b, c). It separates the Le Danois Drift from the bank along a WNW-ESE linear trend (Fig. 5).
263 The Le Danois Moat is about 42 km long. It has a U-shaped profile with widths ranging from 1.9 to 2.2 km
264 and depths from 20 to 80 m (Figs. 6a, c). Towards the west, the moat narrows to a minimum width of 400
265 m.

266 The NW-SE oriented Gijón Moat separates the Gijón Drift from the upper continental slope (Fig. 5). This
267 moat (from 320 to 1090 m) starts at the southern foot of the Vizco High and extends towards the Lastres
268 Canyon. It deflects to the southeast and loses expression to the east. The northwest part of the moat shows
269 an asymmetric U-shape profile (Figs. 6a, b, d) and has a depth ranging from 25 to 110 m, a width of about
270 2.3 km. Towards the southeast, the moat narrows to a minimum width of 800 m and the depth reduces to
271 10 to 20 m.

272 The Asturias Moat is associated with the Asturias Drift (Fig. 5). It is oriented in a W-E direction in the
273 western part and becomes NNW-SSE towards its NE limit. The moat is about 6 km long, 400 m wide, 80 m
274 deep and displays a V-shape profile (Fig. 6c).

275 A NW-SE oriented furrow occurs at the southwest edge of the Gijón Drift (Fig. 5). It can be identified on
276 the multibeam bathymetry (Figs. 2, 4a) and seismic reflection profiles (Fig. 6b) by its vertical incision,
277 ranging from 10 to 20 m. The length is 4.1 km and the width is 0.8 km. It gradually loses its expression
278 towards the southeast, as well as towards the Vizco High.

279 4.2 Downslope features

280 Four isolated small slide scars are identified along the southern flank of the Le Danois Bank (Fig. 5).
281 They possess relatively steep slopes (values between 6° and 18°) compared to the surrounding seafloor
282 (values between 1° and 4°) (Fig. 3). They are characterized by crescent shapes, lengths varying between
283 1.3 and 3.2 km, depths ranging between 20 and 80 m and south-dipping orientations. All of the slide scars
284 are present between 544 and 1020 m water depth (Fig. 3). The slide scars located at plastered drift 4
285 (from 840 to 877 m, slope gradient of 12°) and central part of the southern flank of the bank (from 803 to
286 854 m, slope gradient of 15°) are namely documented by Figures 6c and 7a.

287 Along the southern rim of the top of the Le Danois Bank, one large isolated slide scar with a steep slope
288 gradient of 15° to 20° has been identified (Figs. 3, 5, 7b, 8a). The headwall, between 565 and 681 m, is
289 characterized by a linear geometry (Fig. 5). This W-E orientated slide scar is about 33 km long and has a
290 mean depth of 90 m.

291 Along the southern flank of the Le Danois Moat, between 990 and 1120 m water depth, two slide scars
292 are identified based on their arcuate morphology (Figs. 3, 5, 7b). Compared to the entire southern flank

293 (mean slope gradient of 2.5°) of the Le Danois Moat, both slide scars are located on the steepest slopes (7°
294 to 9.5° slope). The eastern scar (2.2 km long and 60 m deep) has a north-dipping trend and an average
295 slope gradient of 8.2° . The western one (3.4 km long and 30 m deep) displays a lower slope gradient of 7.8°
296 with a northeast-dipping trend. Their associated slide deposits are characterized by onlap and downlap
297 terminations overlying an unconformity surface (Fig. 7b).

298 At the centre of the intraslope basin, a 2.7 km^2 isolated ellipse-shaped slide scar is shown on the
299 bathymetric and seismic data (Figs. 3, 5, 8b). This well-developed seafloor scarp shows a higher slope
300 gradient (3.5°) compared to the surrounding slopes (1.5°). It has a northeast-dipping trend and gradually
301 loses its expression from southwest to northeast (Figs. 3, 5). The headwall, located between 750 to 777 m
302 water depth, is about 2.5 km long and displays truncated seismic reflection configurations in the seismic
303 records. At the bottom of this slide scar, chaotic-transparent seismic reflections are present (Fig. 8b).

304 A series of isolated slide scars have been identified southeast of the Vizco High between 870 and 1280 m
305 water depth (Figs. 5, 8c). They are positioned on an erosive unconformity surface and display a step-like
306 pattern with at least 5 levels (at 1070, 1010, 960, 940 and 920 m) (Fig. 8c). These slide scars have an east-
307 dipping trend and gradually lose their expressions from the west to the east. The seismic facies of these
308 features are truncated reflections at their headwalls and chaotic-transparent reflections at the bottom.
309 They have small variations in shape (arcuate), size (2.8 to 3.2 km in diameter, 20 to 60 m deep) and
310 orientation (N-S) (Fig. 5). The slope gradient of the headwalls ranges from 7° to 13° (Fig. 3).

311 A large area (233 km^2) of mass-transport deposit is located between the Le Danois Drift, the Gijón Drift
312 and the Lastres Canyon (Fig. 5). The identification is based on a distinctive seafloor irregularity and
313 discontinuous low-amplitude chaotic and transparent reflections in the seismic records (Fig. 8d). The
314 boundary of these mass-transport deposits has a relatively sharp slope gradient (about 4.5°) compared to
315 the surrounding area (about 0.8°) (Fig. 3).

316 4.3 Topographic irregularities and morphological depressions

317 At the northeast edge of the Gijón Moat, an ellipse-shaped morphological depression (about 20 m deep)
318 is identified between 680 and 770 m water depth (Fig. 8e). It is 5.5 km in diameter and 30 to 80 m deep
319 with a NW-SE orientation. The scarp is characterized by an erosive unconformity surface and truncated

320 reflections. Undulating wavy-oblique reflections make up the succession between the seafloor and the
321 unconformity surface in the seismic records. The wave-crest features are about 1-2 km long, 200 m wide
322 and rise 10 m above the surrounding areas with a trend of upslope migration. The wave ridges have a NE-
323 SW orientation.

324 At the centre of the intraslope basin, a remarkable asymmetric ear-shaped depression is identified
325 between 990 and 1080 m water depth (Figs. 5, 8f). It is 6 km in diameter and has a northwest-dipping
326 trend. The upslope facing flank is 20 to 90 m deep with a slope gradient of about 18° (Fig. 3). It is
327 characterized by truncation of parallel-stratified reflections (Fig. 8f). This depression delimits an oblique
328 terrace (2.3° slope) with wavy morphology along the downslope facing flank. The related terrace displays
329 high-amplitude chaotic reflections overlain by continuous wavy-stratified reflections (Fig. 8f). These
330 wave-like features are about 2.5-3.5 km long, 400 m wide and rise 30 m above the surrounding seafloor.
331 The wave ridges have a N-S orientation.

332 Several topographic irregularities and morphological depressions (from 1540 to 2100 m) occur
333 between the Le Danois Drift, plastered drift 6 and the Lastres Canyon. The identification is based on their
334 irregular shapes (circular, crescent and ellipse-shaped), sizes (0.8 to 3.7 km in diameter, 40 to 80 m deep),
335 slope gradients (values between 15° and 22°) and orientations (WSW-ENE to NW-SW trending) (Figs. 3,
336 5). Only a few seismic profiles document these depressions. They are characterized by truncated, chaotic,
337 semi-transparent or wavy-stratified reflections (Fig. 7e).

338 **5 Discussion**

339 **5.1 Present-day bottom-current implications on contourite features**

340 The present-day bottom-current circulation within the Le Danois intraslope basin is dominated by three
341 water masses: the ENACW, the AMW and the LSW. Due to their different physical characteristics and
342 circulation patterns, they may play a significant role in shaping the present-day depositional and erosional
343 contourite features. The combination of the CTD data (World Ocean Database, 2013) and the interpreted
344 seismic profiles (Figs. 6, 7, 8) allow gaining more insights regarding the interaction between each water
345 mass and its impact on the local seabed (contouritic) processes.

346 5.1.1 ENACW related processes

347 The ENACW (flowing between 200 and 570 meter water depth) mainly interacts with the upper
348 continental slope and the upper southern flank of the Le Danois Bank, where plastered drifts 1 and 2, 3 are
349 respectively located (Figs. 9a, b, c). Present-day bottom currents along the southern flank of the bank in
350 that depth interval are approximately 15 cm/s (González-Pola et al., 2012). Along the Asturias continental
351 slope, the ENACW generally has a mean velocity of 10-30 cm/s (González-Pola et al., 2012). All of these
352 values meet the conditions (Stow et al., 2002, 10-30 cm/s) for generating plastered geometry of
353 contourite drifts 1, 2, 3, and related bottom currents are most likely resulted from the ENACW circulation
354 documented by González-Pola et al. (2012) (Fig. 10). Additionally, plastered drifts 2 and 3 are distributed
355 along the northern and southern foot of a ridge (Fig. 7a) with similar orientations, shapes and lengths.
356 These features illustrate similar bottom-current processes resulting from interactions between small flow
357 filaments and the adjacent topographic obstacle. The related bottom-current dynamics could be compared
358 with the present-day anticyclonic circulation cell along the western rim of the Le Danois Bank (González-
359 Pola et al., 2012) (Fig. 10).

360 Gentle slope morphology is one of the main elements responsible for the formation of plastered drifts as
361 well (Laberg and Camerlenghi, 2008). At the eastern edge of plastered drifts 2 and 3, the slope gradient
362 abruptly increases to 8.5°. This steep slope is maintained to the southeast flank of the bank (Fig. 3). Higher
363 slope gradients could accelerate bottom currents, in turn shifting sedimentary processes from deposition
364 to non-deposition/erosion (Rebesco et al., 2014). These higher slope angles could inhibit the generation of
365 plastered drifts along this part of the Le Danois Bank. Towards the eastern boundary of plastered drift 1,
366 the slope gradient maintains but the space between the lower continental slope and the Asturias
367 continental shelf is widened (Fig. 3). The wide morphology will decelerate bottom currents (Faugères and
368 Stow, 2008). Slower flows could limit the lateral extension of plastered drift 1 towards the east.

369 5.1.2 AMW related processes

370 The AMW mainly interacts with the southern flank of the Le Danois Bank and the intraslope basin
371 between 750 and 1500 m water depth (Fig. 9). Plastered drift 4 (from 870 to 1100 m) is positioned along
372 the upper southeast flank of the Le Danois Bank (Figs. 7b, 9d), where bottom currents are estimated at 10-

373 15 cm/s (González-Pola et al., 2012). This drift covers a gentle slope (mean slope gradient of about 3.6°)
374 (Fig. 3) and is shaped by the AMW (Fig. 10). Along the entire boundary of plastered drift 4, the slope
375 gradients abruptly increase to 8-15° (Fig. 3), delineating its extent. Considering all, slope morphology is
376 the main controlling factor for the spatial distribution of plastered drift 4.

377 The Le Danois Drift (from 790 to 1080 m) is suggested to be generated by the AMW as well. The
378 associated Le Danois moat indicates a focused flow pathway of bottom currents all along the southern foot
379 of the Le Danois Bank. This feature matches with the present-day oceanographic data documented by
380 González-Pola et al., (2012). A 12-month long mooring record (at 44°02.33', N 4°49.33' W) indicates a
381 persistent westward near-bottom flow along the southern foot of the bank at the AMW level (González-
382 Pola et al., 2012). Direct current measurements at this level, consisting of few snapshots made by landers,
383 fit with the velocity in the range of 10-25 cm/s (González-Pola et al., 2012). This velocity is sufficient to
384 generate associated contourite drifts (Stow et al., 2002, 2009). Towards its western limit, the Le Danois
385 Drift extends to an open area between the lower continental slope and the intraslope basin (Fig. 5). In this
386 area, the Le Danois bank is absent and bottom currents most likely will drop to the reported background
387 values, which are less than 5 cm/s (Iorga and Lozier, 1999a). Towards the eastern limit of this drift, the
388 presence of a group of morphological depressions limits the distribution of the Le Danois Drift (Fig. 5).
389 Consequently, slower bottom currents and seabed morphology limit the distribution of the Le Danois Drift.
390 The Le Danois Drift and plastered drift 4 have similar orientations and are located at the same water
391 depths (Figs. 5, 10). The distribution suggests that the associated bottom-current processes of both drifts
392 are related to the same current (Fig. 10). The presence of two types of contourite drifts along the AMW
393 pathway can be explained by changes in current velocities (Faugères and Stow, 2008). This implies
394 accelerated and then decelerated processes from the southeast towards the southwest flank of the Le
395 Danois Bank.

396 The Gijón Drift and the Moat extend from 320 to 1090 m water depth. A CDS is usually associated with
397 one water mass (Rebesco et al., 2014). However, at the present day, the Gijón Drift is situated within the
398 boundaries of two different water masses, being the ENACW and the AMW (Figs. 9a, b, c). Along the
399 Cantabrian continental upper slope, the ENACW does not reach to 1000 m for prolonged periods of time
400 (McCartney and Mauritzen, 2001), while the AMW could only reach up to 400 m during interglacial
401 climate cycles (Zhang et al., 2016; Kaboth et al., 2016, 2017). Additionally, shape and morphology of the

402 Gijón Drift display different features in different depth intervals. Within the ENACW, the Gijón Drift has
403 elongated and mounded geometry (Figs. 9b, c), whereas the part within the AMW is confined and
404 mounded (Fig. 9a). Different shapes of contourite drifts are related to different bottom-current conditions
405 (Faugères and Stow, 2008). As such, it is possible that the ENACW and the AMW interacted with the upper
406 continental slope during different climate intervals and both are responsible for the Gijón Drift.

407 The spatial variation of the Gijón Drift could be controlled by the slope morphology as well. On the
408 multibeam bathymetry, the Gijón Moat (NE-SW trending) does not fit the alongslope distribution
409 compared to the Asturias continental slope (WNW-ESE trending) (Figs. 4a, 5). The obliquity may be
410 caused by the presence of the Gijón Canyon (NE-SW trending) (Figs. 5, 9f). Interactions between canyon
411 channels and bottom currents are possible to provoke streamline distortions and accelerate current flows
412 (Holland, 1972). The related distortion and acceleration enable bottom currents flowing upwards along
413 canyon channels (Jackson et al., 2006). When the AMW encounters the Gijón Canyon, bottom currents
414 could follow the canyon morphology (Allen and De Madron, 2009; Muench et al., 2009) and arise towards
415 the shallower continental slope (320 m water depth). The variation of the Gijón Drift could also link with
416 the interaction between the Gijón Canyon and the AMW.

417 The Asturias Drift lies around a buried structural high at the centre of the intraslope basin (Figs. 5, 6c,
418 9c). The presence of a topographical obstacle can create faster currents, in turn generating contourite
419 depositional and erosional features (Ercilla et al., 2016; García et al., 2016). The associated Asturias Moat
420 indicates the pathway of bottom currents. The W-E to NNW-SSE deflection of the moat may result from
421 the morphological control of the associated depression (Fig. 10). As such, the Asturias Drift and Moat
422 result from interactions of the AMW with a buried structural high and a morphological depression.
423 Related bottom-current processes could be linked with the present-day AMW circulation cell (González-
424 Pola et al., 2012) in the intraslope basin (Fig. 10).

425 At the southeast edge of a group of slide scars, a furrow is located in the Gijón Drift at water depths of
426 844 to 870 m (Figs. 5, 6b). Present-day bottom currents associated with the AMW in the intraslope basin
427 (from 10 to 20 cm/s, González-Pola et al., 2012) do not have sufficient energy to create erosive furrows,
428 which require at least 30 cm/s (Stow et al., 2009). However, it is well documented that the presence of
429 topographic obstacles or irregularities can cause locally intensified bottom currents (Rebesco et al., 2008,

430 2014). Examples include the Galicia Bank region where (numerically modelled) intensifications from 7
431 cm/s up to 35 cm/s are recorded (Zhang et al., 2016), the Porcupine Abyssal Plain where accelerations
432 reach 15 cm/s (Turnewitsch et al., 2004), and the Xisha Trough where (also numerically modelled)
433 enhancements from 15 cm/s up to 30 cm/s are documented (Chen et al., 2016). Similarly, bottom currents
434 can recirculate around the Vizco High, possibly speeding up from 10-20 cm/s to over 30 cm/s in this
435 region. The presence of the furrow indicates faster bottom currents resulted from strong interactions with
436 the Vizco High.

437 5.1.3 LSW related processes

438 The LSW is only present between the Lastres Canyon and the lower southern flank of the Le Danois
439 Bank in the study area (below 1750 m water depth) (Figs. 4f, 9). Plastered drifts 5 is located along the
440 lower southern flank (2.4° slope) while plastered drift 6 lies along the southeastern foot (1.2° slope) of the
441 bank (Figs. 3, 5, 9e). Both lay within the depth windows of the LSW. Along the Cantabrian continental
442 slope, the bottom current velocities (2-6 cm/s; Speer et al., 1999; Friocourt et al., 2007) are below the
443 threshold for depositing plastered drifts (Stow et al., 2002, 2009). Consequently, the presence of these two
444 plastered drifts indicates local intensification. Since there are no known measurements of current
445 velocities at this depth interval in the study area, tentative bottom-current velocities generating these
446 plastered drifts have to be estimated in order to better understand the acceleration of bottom currents in
447 a topographically constrained basin. Since the average threshold for deposition of plastered drifts has
448 been indicated at 10 cm/s (Stow et al., 2009), we thus estimate the local current velocities must exceed
449 this value. Along the entire boundary of plastered drift 5, slope gradients increase to 6°-10° (Figs. 3, 5). As
450 such, steeper slope morphologies control and limit the distribution of plastered drift 5. The extension of
451 plastered drift 6 is limited by seafloor depressions positioned between the bank and the Lastres Canyon
452 (Fig. 5). Towards the northeast boundary of plastered drift 6, the presence of a topographic high locally
453 creates slopes from 1° to 11° (Fig. 3). These slopes limit the distribution of plastered drift 6.

454 5.2 Interaction with slope instability processes

455 In the study area, plenty of slide scars occur at the surfaces of contourite drifts and along the southern
456 flank of the Le Danois Bank (Figs. 2, 3, 5). The main causal factors for submarine slides include high slope

457 angles, seismic activity, volcanic activity, gas charging and rapid sediment accumulation (Locat and Lee,
458 2002; Sultan et al., 2004; Verdicchio and Trincardi, 2008; Miramontes et al., 2016; Rashid et al., 2017).
459 Since no seismic or volcanic activity and gassy sediments have been observed in the study area, the
460 triggering mechanisms for these slide scars are either rapid sediment accumulation or oversteeping.

461 5.2.1 Increased sediment accumulation

462 An isolated slide scar is positioned at the northeast part (3° slope) of the Gijón Drift (Figs. 2, 3, 8b). The
463 sedimentation rate of the Gijón Drift is unknown. However, mounded drifts are known to have relatively
464 high sedimentation rates (5-60 cm/ka) compared to pelagic (<2 cm/ka) and hemipelagic (5-15 cm/ka)
465 sediments (Stow et al., 2008). During the build-up of the Gijón Drift, high sedimentation rates are capable
466 of decreasing shear strength of sediments, favouring the formation of mass-wasting events (Baeten et al.,
467 2013). Since the slide scar lies between the Asturias Drift and the Gijón Drift (Fig. 5), two drift systems can
468 deliver sediments to this location and drastically increase the sedimentation rate. As such, the occurrence
469 of a slope instability event at this location is more likely, compared to other areas of the Gijón Drift.

470 Opposed to the Gijón Drift, no slope instability processes occur at the surface of the Le Danois Drift (Figs.
471 2, 3, 5). The difference between both drifts may be related to their internal depositional structures.
472 Interbedded continuous sigmoidal reflections and discontinuous low-amplitude chaotic reflections within
473 the Gijón Drift are interpreted as interbedded mass-transport and contourites deposits (Figs. 6a, d),
474 whereas only contourites are present within the Le Danois Drift (Figs. 6a, c). These interbedded features
475 are mainly located at the Gijón Moat, indicating multiple shifts between alongslope and downslope
476 processes over the Gijón Drift. Different degree of sedimentary sorting, resulting from distinct
477 sedimentary processes, could lead to the deposition of different sedimentation layers (Wilson et al., 2004).
478 These sedimentation layers generally have higher sensitivity, due to their distinct physical properties
479 (Laberg and Camerlenghi, 2008). Higher sensitive layers can effectively reduce shear resistance strength
480 of sedimentary bodies and thus a dynamic slide process can initiate (Kvalstad et al., 2005). Similar
481 examples have been documented in the vicinity of the Storegga Slide region (glacigenic/contouritic
482 deposits), offshore Norway (Bryn et al., 2005) and in the Afen Slide area (mud/sand contouritic deposits),
483 offshore UK (Wilson et al., 2004). Within the Gijón Drift, multiple shifts between alongslope and

484 downslope processes create high sensitive layers and induce mass movements. Conversely, the shear
485 strength of the Le Danois Drift is not low enough to trigger slope instability events.

486 Between the northwest end of the Gijón Drift and the Vizco High, a series of slide scars overlay a steep
487 slope (10°) (Figs. 2, 3, 8c). Thick contourite deposits of the Gijón Drift, as well as steep slope morphology
488 could have a significant potential for producing mass movements.

489 5.2.2 Scouring of active bottom currents

490 Two slide scars occur at the southern flank of the Le Danois Moat (Figs. 2, 3, 5). Both slide scars are
491 distributed along the steepest (9°) parts of the moat (Fig. 3). The focused flow within the Le Danois Moat
492 could be held responsible for the formation of these slide scars. Similar to the Cape Basin, where a slide
493 scar is induced by scouring of bottom currents (Weigelt and Uenzelmann-Neben, 2004), higher angles and
494 active bottom currents can provide favourable conditions for slope instability processes in this part of the
495 moat. The associated slide deposits display internal structures with onlap and downlap terminations and
496 their geometry resemble patched drift features (Fig. 7b), hinting towards reworking of bottom currents.
497 The observed features in the study area are similar to recent discoveries in the Guadalquivir Bank, where
498 reworking of bottom currents reshaped the slide deposits (García et al., 2016). In conclusion, focused
499 bottom currents within the Le Danois Moat locally scour the steeper flank, this may lead to undercutting
500 of the slope, triggering mass movements.

501 5.2.3 Mixed processes

502 In the Le Danois Bank region, a large area of mass-transport deposits lies between the Lastres Canyon,
503 the Gijón and the Le Danois Drifts (Fig. 5). The associated scarp is about 10 km away from the Lastres
504 canyon channel (Figs. 2, 3). The seafloor morphology of the mass-transport deposits shows an upslope
505 trending from the canyon wall towards the scarp. As such, turbidity currents associated with the Lastres
506 canyon are not possible to penetrate (10 km) upslope undercutting the scarp, and are most likely not
507 responsible for the formation of these mass-transport deposits. The slope gradient (9.5°) of this location is
508 much higher than the surrounding seafloor (2.8°) (Fig. 3). High slope angles lead to downslope processes
509 at this particular location. Towards the east, the orientation of this mass-transport deposits area gradually

510 changes from downslope (N-S trending) to alongslope (W-E trending) directions (Fig. 5). This deflection
511 indicates the interaction between mass movements and AMW currents (Fig. 10). Characteristics of these
512 mass-transport deposits can be compared to those at the southeast Grand Banks (Rashid et al., 2017) and
513 along the Mid-Norwegian Margin (Bryn et al., 2005), where the area of mass-transport deposits is
514 elongated and enlarged and the related distribution and location are highly influenced by bottom currents.
515 As such, a high slope gradient could be predisposing factors for the formation of these mass-transport
516 deposits and bottom currents resulting from the AMW highly controls their distribution.

517 5.3 A genetic model for the sediment waves of the Le Danois Bank region

518 Within the intraslope basin, wavy features are identified in the seismic records (Figs. 7e, 8e, f). These
519 features are interpreted as sediment wave fields (respectively A, B and C on Fig. 5) based on the traceable
520 and continuous seismic reflections, as opposed to slope failure deposits with sharp and acoustically
521 incoherent reflections (Gardner et al., 1999; Lee et al., 2002; Mosher and Thomson, 2002; Wynn and Stow,
522 2002). The formation of sediment waves has three possible causes, being turbidity currents, bottom
523 currents or internal waves (Ercilla et al., 2002; Ribó et al., 2016). Turbidity-current related sediment
524 waves generally occur on the back-slopes of channel levees and in turbidity-current channels (Wynn and
525 Masson, 2008). Since the study area with sediment waves lacks the presence of channel-levee systems and
526 turbidity-current processes, these sediment wave fields most likely result from bottom currents or
527 internal waves.

528 Sediment wave field A is located within the AMW level and is induced by internal waves. Bottom
529 currents can be ruled out as the moat in the vicinity of sediment wave field A suggests N-S oriented
530 bottom currents (Fig. 10), which is parallel to the wave crests. This orientation does not fit the bottom-
531 current induced sediment waves (oblique or perpendicular orientations of the wave crests; Masson et al.,
532 2002; Wynn and Masson, 2008).

533 Sediment waves created by internal waves are documented in several regions (Pomar et al., 2012;
534 Delivet et al., 2016; Ribó et al., 2016). When internal waves propagate down a sloping bottom, three
535 possible reflection conditions exist based on the propagation angle of the internal wave (c) and the bottom
536 slope angle (γ) (Cacchione et al., 2002). The relationship was established by Cacchione and Wunsch (2006)
537 and can be written as:

$$c = \arctan \left[\left(\frac{\sigma^2 - f^2}{N^2 - \sigma^2} \right)^{\frac{1}{2}} \right]$$

538 where σ is the internal wave frequency, f is the local Coriolis (inertial) frequency, and N is the Brunt-
 539 Väisälä (buoyancy) frequency. Different values of γ/c correspond to subcritical ($\gamma/c < 1$), critical ($\gamma/c \approx 1$)
 540 and supercritical ($\gamma/c > 1$) reflection conditions (Lamb, 2014). In the study area, high-frequency internal
 541 waves have been observed near the centre of the intraslope basin at the level of the AMW (González-Pola
 542 et al., 2012). Based on the local flow properties, González-Pola et al. (2012) proposed the following
 543 parameters: f as 1.013×10^{-4} /s, σ as 0.09 cph and N as 1.5 to 2.5×10^{-3} s⁻¹. Thus, internal wave reflection
 544 condition in sediment wave field A (1.6° slope) is subcritical. Subcritical conditions of internal waves are
 545 generally characterized by smaller wave heights and upslope migration (Lamb, 2014; Delivet et al., 2016;
 546 Ribó et al., 2016). And this is true for sediment wave field A, which migrates upslope and their wave
 547 heights is relatively small (10 m) compared to those in the Argentine Basin (30 m) (von Lom-Keil et al.,
 548 2002), the Gulf of Valencia (50 m) (Ribó et al., 2016) and the Bahama Outer Ridge (60 m) (Flood and
 549 Giosan, 2002).

550 Sediment wave fields B (Fig. 9f) and C (Fig. 9g) are respectively located at the ENACW/AMW and the
 551 AMW/LSW interfaces. No mooring measurements have been performed at these interfaces and the
 552 present-day oceanographic dynamics are unknown. However, the mean salinity values at the
 553 ENACW/AMW (35.6) and the AMW/LSW interfaces (35.2) (Fig. 9) indicate mixing processes as the
 554 ENACW has a mean salinity of 35.5, the AMW 35.8 and the LSW 35.1 (Fig. 4b). Turbulent mixing at the
 555 interface between water masses generally produces relatively high energetic currents associated with
 556 internal waves, which are capable of transporting and depositing sediments (Preu et al., 2013; Ercilla et al.,
 557 2016; Juan et al., 2016). Based on the local flow properties (González-Pola et al., 2012), internal wave
 558 reflection conditions in sediment wave fields B (1.6° slope) and C (1.7° slope) are subcritical. The
 559 relatively small wave heights (7 and 10 m for wave fields B and C) and the observed upslope migration
 560 both indicate a subcritical reflection parameter (Lamb, 2014). As such, sediment wave fields B and C are
 561 most likely related to internal waves as well. Both sediment wave fields are located within morphological
 562 depressions (slopes of 8°-10°) (Figs. 3, 5) and overlie irregular unconformity surfaces (Figs. 7d, 8c), which
 563 are the prerequisites for the formation of sediment waves (Aghsaee et al., 2010).

564 5.4 Sediment sources

565 The sediments constituting the various drifts in the region are mainly transported by downslope
566 processes to the continental slopes and caught by bottom currents from adjacent areas towards the Le
567 Danois Bank region (Gómez-Ballesteros et al., 2014). One year long current meter data, obtained from the
568 Avilés Canyon (west of the Le Danois area, Fig. 1a) indicates direct delivery of river-sourced (the Narcea
569 and Nalon Rivers) material into the canyon and its adjacent continental slope (Rumín-Caparrós et al.,
570 2013). Frequent severe storms and repeated cycles of semidiurnal tides regionally enhanced the bottom
571 currents, assuring a permanent amount of sediment in suspension in the canyon region (Rumín-Caparrós
572 et al., 2016). Additionally, the Narcea and Nalon Rivers are generated before the formation period (the
573 Neogene, Gómez-Ballesteros et al., 2014) of the Avilés canyon (Fernández-Viejo et al., 2014). The
574 suspended material is possible to be picked up by eastward moving water masses towards the Le Danois
575 Bank since the intensification of the AMW (during the late Pliocene, Hernández-Molina et al., 2014) and
576 the establishment of the Iberian Poleward Current (during the late Pleistocene, Mena et al., 2018).
577 Consequently, the Narcea and Nalon Rivers could provide sediments for identified contourite deposits for
578 prolonged periods of time (Gómez-Ballesteros et al., 2014; Rumín-Caparrós et al., 2016).

579 The Avilés Canyon is not the only sediment source for the contourite deposits. Current meter data
580 reveal a long-term (12-month) persistent westward flow within the Le Danois Moat (González-Pola et al.,
581 2012), which has an opposite direction compared to the major branch of the AMW (Fig. 10). Additionally,
582 the LSW flows towards the intraslope basin in a westward direction as well (Fig. 10). These observations
583 suggest an additional eastern sediment source should be present. The Torrelavega Canyon is located in
584 the vicinity of the study area and fed by sediments from the Besaya River (Fig. 1a) (Caballero et al., 2014).
585 Eddies extending from the surface down to 3500 m water depth have been observed above the
586 Torrelavega canyon (Caballero et al., 2014), which remained stationary for a long time (locally up to 7
587 months) (Pingree and Le Cann, 1992; Caballero et al., 2014), creating the possibility for associated
588 energetic current patterns to erode the seafloor and suspend sediments (Shanmugam, 2013). As such,
589 suspended sediments can be transported towards the Le Danois Bank area by bottom currents associated
590 with the AMW and the LSW.

591 The Gijón and the Lastres Canyons can be possible sediment sources as well. Few studies have
592 documented these two canyon systems. Based on their locations, the Sella River is suggested to be the

593 sediment supply for both canyons (Fig. 1a). Erosive features at the canyon walls have been displayed in
594 the seismic records (Fig. 9f). Due to the consistent AMW flowing above the intraslope basin, eroded
595 sediments can contribute to the sediment accumulation of the prevailing contourite drifts. Finally, mass-
596 transport deposits are interbedded within the Gijón Drift (Figs. 6a, d) and indicate the interaction between
597 bottom currents and gravitational processes along the upper continental slope. These processes may add
598 sediments from the Asturias continental shelf to the contourite drifts.

599 **6 Conclusion**

600 The spatial variability of contourite drifts, slope morphology and small-scale bottom-current processes
601 are all tied together in this topographically constrained small basin. Bottom currents associated with the
602 ENACW, the AMW and the LSW are more focused and strongly intensified (estimated acceleration up to 25
603 cm/s) due to the morphological constraint of the Le Danois Bank and the Vizco High. Changes in velocities
604 of bottom currents and slope gradients result in variations in types, shapes and spatial distributions of
605 contourite drifts, especially along the current pathways of the AMW. Unlike typical elongated and
606 mounded drifts, the Gijón Drift exhibits a lateral variation (evolving from elongated to confined geometry)
607 at different depth intervals, which evidently indicate different bottom-current dynamics associated with
608 one contourite drift, suggesting specific geometries and shapes of contourite drifts in topographically
609 constrained small basins. Despite the influence of large topographic obstacles, small steep (slopes of 8°-
610 10°) morphologic irregularities may interact with internal waves, generating small-scale (wave heights 7-
611 10 m) upslope-migrated sediment waves in the intraslope basin. Enhanced bottom-current processes
612 interplay with internal waves and slope instability events, and determine the complex morphology of the
613 present-day seafloor. Compared with large contourite features resulted from deep water masses, small
614 basin-scale contourite features of the Le Danois Bank region is an exquisite example of multiple processes
615 interacting in a topographically constrained basin at an intermediate water depth. The spatial variability
616 of the contourite features is more frequent than anticipated so far and can have far-reaching implications
617 for comparable topographic and oceanographic settings all over the world.

618 **Acknowledgements**

619 This study was carried out within the framework of a Chinese Scholarship Council “CSC Grant”
620 (201506410062). The research was conducted in collaboration with “The Drifters Research Group” of the

621 Royal Holloway University of London (UK) and it is related to the projects CTM 2012-39599-C03,
622 CGL2016-80445-R, and CTM2016-75129-C3-1-R. The authors wish to express our gratitude to the crews
623 and scientific researchers of the MARCONI II, the ECOMARG, the CONTOURIBER and the R/V Belgica
624 ST1118a campaigns. Shiptime RV Belgica was provided by BELSPO and RBINS-OD Nature. These research
625 campaigns framed within the ECOMARG (REN2002-00916/MAR) and MARCONI (REN2001-1734 C03-
626 01/M) projects. This study also builds upon achievements of project ESF Euromargins MOUNDFORCE, EC
627 FP5 RTN EURODOM and EC FP6 HERMES (GOCE-CT-2005-511234-1).

628 **References**

- 629 Aghsaee, P., Boegman, L., Lamb, K.G., 2010. Breaking of shoaling internal solitary waves. *J Fluid Mech* 659, 289–317.
630 <https://doi.org/10.1017/S002211201000248X>
- 631 Allen, S.E., Durrieu De Madron, X., 2009. A review of the role of submarine canyons in deep-ocean exchange with the
632 shelf. *Ocean Sci* 5, 607–620. <https://doi.org/10.5194/os-5-607-2009>
- 633 Alvarez-Marrón, J., Pérez-Estaún, A., Dañobeitia, J.J., Pulgar, J.A., Martínez Catalán, J.R., Marcos, A., Bastida, F., Ayarza
634 Arribas, P.A., Aller, J., Gallart, A., Gonzalez-Lodeiro, F., Banda, E., Comas, M.C., Córdoba, D., 1996. Seismic
635 structure of the northern continental margin of Spain from ESCIN deep seismic profiles. *Tectonophysics* 264,
636 153–174. [https://doi.org/10.1016/S0040-1951\(96\)00124-2](https://doi.org/10.1016/S0040-1951(96)00124-2)
- 637 Baeten, N.J., Laberg, J.S., Forwick, M., Vorren, T.O., Vanneste, M., Forsberg, C.F., Kvalstad, T.J., Ivanov, M., 2013.
638 Morphology and origin of smaller-scale mass movements on the continental slope off northern Norway.
639 *Geomorphology* 187, 122–134. <https://doi.org/10.1016/j.geomorph.2013.01.008>
- 640 Boillot, G., Dupeuble, P.A., Malod, J., 1979. Subduction and tectonics on the continental margin off northern Spain. *Mar*
641 *Geol* 32, 53–70. [http://dx.doi.org/10.1016/0025-3227\(79\)90146-4](http://dx.doi.org/10.1016/0025-3227(79)90146-4)
- 642 Bryn, P., Berg, K., Stoker, M.S., Haflidason, H., Solheim, A., 2005. Contourites and their relevance for mass wasting along
643 the Mid-Norwegian Margin, in: Ormen Lange—an Integrated Study for Safe Field Development in the Storegga
644 Submarine Area. Elsevier, Oxford, pp. 85–96. <https://doi.org/10.1016/B978-0-08-044694-3.50011-1>
- 645 Caballero, A., Ferrer, L., Rubio, A., Charria, G., Taylor, B.H., Grima, N., 2014. Monitoring of a quasi-stationary eddy in the
646 Bay of Biscay by means of satellite, in situ and model results. *Deep Sea Res Part II Top Stud Oceanogr* 106, 23–
647 37. <https://doi.org/10.1016/j.dsr2.2013.09.029>
- 648 Cacchione, D., Wunsch, C., 2006. Experimental study of internal waves over a slope. *J Fluid Mech* 66, 223–239.
649 <https://doi.org/10.1017/S0022112074000164>
- 650 Cacchione, D.A., Pratson, L.F., Ogston, A.S., 2002. The Shaping of Continental Slopes by Internal Tides. *Science* (80) 296,
651 724–727. <https://doi.org/10.1126/science.1069803>
- 652 Cartes, J.E., Huguet, C., Parra, S., Sanchez, F., 2007. Trophic relationships in deep-water decapods of Le Danois bank
653 (Cantabrian Sea, NE Atlantic): Trends related with depth and seasonal changes in food quality and availability.
654 *Deep Sea Res Part I Oceanogr Res Pap* 54, 1091–1110. <https://doi.org/10.1016/j.dsr.2007.04.012>
- 655 Chen, H., Xie, X., Van Rooij, D., Vandorpe, T., Su, M., Wang, D., 2014. Depositional characteristics and processes of
656 alongslope currents related to a seamount on the northwestern margin of the Northwest Sub-Basin, South
657 China Sea. *Marine Geology*, 355, 36–53. <http://dx.doi.org/10.1016/j.margeo.2014.05.008> Chen, H., Xie, X., Zhang,
658 W., Shu, Y., Wang, D., Vandorpe, T., Van Rooij, D., 2016. Deep-water sedimentary systems and their relationship
659 with bottom currents at the intersection of Xisha Trough and Northwest Sub-Basin, South China Sea. *Mar Geol*
660 378, 101–113. <http://dx.doi.org/10.1016/j.margeo.2015.11.002>
- 661 Chen, H., Zhang, W., Xie, X., Ren, J., 2019. Sediment dynamics driven by contour currents and mesoscale eddies along
662 continental slope: A case study of the northern South China Sea. *Mar Geol* 409, 48–66.
663 <https://doi.org/10.1016/j.margeo.2018.12.012>
- 664 Delivet, S., Van Eetvelt, B., Monteys, X., Ribó, M., Van Rooij, D., 2016. Seismic geomorphological reconstructions of Plio-
665 Pleistocene bottom current variability at Goban Spur. *Mar Geol* 378, 261–275.
666 <http://dx.doi.org/10.1016/j.margeo.2016.01.001>
- 667 Ercilla, G., Alonso, B., Wynn, R.B., Baraza, J., 2002. Turbidity current sediment waves on irregular slopes: observations
668 from the Orinoco sediment-wave field. *Mar Geol* 192, 171–187. [http://dx.doi.org/10.1016/S0025-3227\(02\)00554-6](http://dx.doi.org/10.1016/S0025-3227(02)00554-6)
- 670 Ercilla, G., Casas, D., Estrada, F., Vázquez, J.T., Iglesias, J., García, M., Gómez, M., Acosta, J., Gallart, J., Maestro-González,
671 A., 2008. Morphosedimentary features and recent depositional architectural model of the Cantabrian
672 continental margin. *Mar Geol* 247, 61–83. <http://dx.doi.org/10.1016/j.margeo.2007.08.007>
- 673 Ercilla, G., Casas, D., Vázquez, J.T., Iglesias, J., Somoza, L., Juan, C., Medialdea, T., León, R., Estrada, F., García-Gil, S.,
674 Farran, M. I., Bohoyo, F., García, M., Maestro, A., 2011. Imaging the recent sediment dynamics of the Galicia Bank
675 region (Atlantic, NW Iberian Peninsula). *Mar Geophys Res* 32, 99–126. <https://doi.org/10.1007/s11001-011-9129-x>
- 677 Ercilla, G., Juan, C., Hernández-Molina, F.J., Bruno, M., Estrada, F., Alonso, B., Casas, D., Farran, M. I., Llave, E., García, M.,
678 Vázquez, J.T., D'Acremont, E., Gorini, C., Palomino, D., Valencia, J., El Moumni, B., Ammar, A., 2016. Significance of
679 bottom currents in deep-sea morphodynamics: An example from the Alboran Sea. *Mar Geol* 378, 157–170.
680 <http://dx.doi.org/10.1016/j.margeo.2015.09.007>

- 681 Faugères, J.C., Stow, D.A. V, 1993. Bottom-current-controlled sedimentation: a synthesis of the contourite problem.
682 *Sediment Geol* 82, 287–297. [http://dx.doi.org/10.1016/0037-0738\(93\)90127-Q](http://dx.doi.org/10.1016/0037-0738(93)90127-Q)
- 683 Faugères, J.C., Stow, D.A. V, Imbert, P., Viana, A., 1999. Seismic features diagnostic of contourite drifts. *Mar Geol* 162, 1–
684 38. [http://dx.doi.org/10.1016/S0025-3227\(99\)00068-7](http://dx.doi.org/10.1016/S0025-3227(99)00068-7)
- 685 Faugères, J.C., Stow, D.A. V, 2008. Chapter 14 Contourite Drifts: Nature, Evolution and Controls, in: Rebesco, M.,
686 Camerlenghi, A. (Eds.), *Developments in Sedimentology*. Elsevier, pp. 257–288.
687 [http://dx.doi.org/10.1016/S0070-4571\(08\)10014-0](http://dx.doi.org/10.1016/S0070-4571(08)10014-0)
- 688 Fernández-Lozano, J., Sokoutis, D., Willingshofer, E., Cloetingh, S., De Vicente, G., 2011. Cenozoic deformation of Iberia:
689 A model for intraplate mountain building and basin development based on analogue modeling. *Tectonics* 30,
690 TC1001. <https://doi.org/10.1029/2010TC002719>
- 691 Flecker, R., Krijgsman, W., Capella, W., de Castro Martins, C., Dmitrieva, E., Mayser, J.P., Marzocchi, A., Modestou, S.,
692 Ochoa, D., Simon, D., Tulbure, M., van den Berg, B., van der Schee, M., de Lange, G., Ellam, R., Govers, R., Gutjahr,
693 M., Hilgen, F., Kouwenhoven, T., Lofi, J., Meijer, P., Sierro, F.J., Bachiri, N., Barhoun, N., Alami, A.C., Chacon, B.,
694 Flores, J.A., Gregory, J., Howard, J., Lunt, D., Ochoa, M., Pancost, R., Vincent, S., Yousfi, M.Z., 2015. Evolution of the
695 Late Miocene Mediterranean–Atlantic gateways and their impact on regional and global environmental change.
696 *Earth-Science Rev* 150, 365–392. <https://doi.org/10.1016/j.earscirev.2015.08.007>
- 697 Flood, R.D., Giosan, L., 2002. Migration history of a fine-grained abyssal sediment wave on the Bahama Outer Ridge.
698 *Mar Geol* 192, 259–273. [http://dx.doi.org/10.1016/S0025-3227\(02\)00558-3](http://dx.doi.org/10.1016/S0025-3227(02)00558-3)
- 699 Friocourt, Y., Levier, B., Speich, S., Blanke, B., Drijfhout, S.S., 2007. A regional numerical ocean model of the circulation
700 in the Bay of Biscay. *J Geophys Res Ocean* 112, C09008. <https://doi.org/10.1029/2006JC003935>
- 701 Frouin, R., Fiúza, A.F.G., Ambar, I., Boyd, T.J., 1990. Observations of a poleward surface current off the coasts of
702 Portugal and Spain during winter. *J Geophys Res Ocean* 95, 679–691.
703 <https://doi.org/doi:10.1029/JC095iC01p00679>
- 704 Gabriela, F.-V., Carlos, L.-F., José, D.-C.M., Patricia, C., 2014. How much confidence can be conferred on tectonic maps of
705 continental shelves? The Cantabrian-Fault case. *Sci Rep* 4, 3661. <https://doi.org/10.1038/srep03661>
- 706 García, M., Hernández-Molina, F.J., Alonso, B., Vázquez, J.T., Ercilla, G., Llave, E., Casas, D., 2016. Erosive sub-circular
707 depressions on the Guadalquivir Bank (Gulf of Cadiz): Interaction between bottom current, mass-wasting and
708 tectonic processes. *Mar Geol* 378, 5–19. <http://dx.doi.org/10.1016/j.margeo.2015.10.004>
- 709 Gardner, J. V, Prior, D.B., Field, M.E., 1999. Humboldt Slide — a large shear-dominated retrogressive slope failure. *Mar*
710 *Geol* 154, 323–338. [https://doi.org/10.1016/S0025-3227\(98\)00121-2](https://doi.org/10.1016/S0025-3227(98)00121-2)
- 711 Gascard, J.C., Clarke, R.A., 1983. The Formation of Labrador Sea Water. Part II. Mesoscale and Smaller-Scale Processes.
712 *J Phys Oceanogr* 13, 1779–1797. [https://doi.org/10.1175/1520-0485\(1983\)013<1779:TFOLSW>2.0.CO;2](https://doi.org/10.1175/1520-0485(1983)013<1779:TFOLSW>2.0.CO;2)
- 713 Gaudin, M., Mulder, T., Cirac, P., Berne, S., Imbert, P., 2006. Past and present sedimentary activity in the Capbreton
714 Canyon, southern Bay of Biscay. *Geo-Marine Lett* 26, 331–345. <https://doi.org/10.1007/s00367-006-0043-1>
- 715 Gómez-Ballesteros, M., Druet, M., Muñoz, A., Arrese, B., Rivera, J., Sánchez, F., Cristobo, J., Parra, S., García-Alegre, A.,
716 González-Pola, C., Gallastegui, J., Acosta, J., 2014. Geomorphology of the Avilés Canyon System, Cantabrian Sea.
717 *Deep Sea Res Part II Top Stud Oceanogr* 106, 99–117. <http://dx.doi.org/10.1016/j.dsr2.2013.09.031>
- 718 González-Pola, C., Díaz del Río, G., Ruiz-Villarreal, M., Sánchez, R.F., Mohn, C., 2012. Circulation patterns at Le Danois
719 Bank, an elongated shelf-adjacent seamount in the Bay of Biscay. *Deep Sea Res Part I Oceanogr Res Pap* 60, 7–21.
720 <http://dx.doi.org/10.1016/j.dsr.2011.10.001>
- 721 Haynes, R., Barton, E.D., 1990. A poleward flow along the Atlantic coast of the Iberian peninsula. *J Geophys Res Ocean*
722 95, 11425–11441. <https://doi.org/10.1029/JC095iC07p11425>
- 723 Hernández-Molina, F.J., Llave, E., Ercilla, G., Maestro, A., Medialdea, T., Ferrin, A., Somoza, L., Gràcia, E., Masson, D.G.,
724 García, M., Vizcaino, A., León, R., 2008. Recent sedimentary processes in the Prestige site area (Galicia Bank, NW
725 Iberian Margin) evidenced by high-resolution marine geophysical methods. *Mar Geol* 249, 21–45.
726 <https://doi.org/10.1016/j.margeo.2007.09.011>
- 727 Hernández-Molina, F.J., Llave, E., Preu, B., Ercilla, G., Fontan, A., Bruno, M., Serra, N., Gomiz, J.J., Brackenridge, R.E.,
728 Sierro, F.J., Stow, D.A. V, García, M., Juan, C., Sandoval, N., Arnaiz, A., 2014. Contourite processes associated with
729 the Mediterranean Outflow Water after its exit from the Strait of Gibraltar: Global and conceptual implications.
730 *Geology* 42, 227–230. <https://doi.org/10.1130/g35083.1>
- 731 Hernández-Molina, F.J., Paterlini, M., Somoza, L., Violante, R., Arecco, M.A., de Isasi, M., Rebesco, M., Uenzelmann-Neben,
732 G., Neben, S., Marshall, P., 2010. Giant mounded drifts in the Argentine Continental Margin: Origins, and global

- 733 implications for the history of thermohaline circulation. *Mar Pet Geol* 27, 1508–1530.
734 <https://doi.org/10.1016/j.marpetgeo.2010.04.003>
- 735 Hernández-Molina, F.J., Wählin, A., Bruno, M., Ercilla, G., Llave, E., Serra, N., Rosón, G., Puig, P., Rebesco, M., Van Rooij, D.,
736 Roque, D., González-Pola, C., Sánchez, F., Gómez, M., Preu, B., Schwenk, T., Hanebuth, T.J.J., Sánchez Leal, R.F.,
737 García-Lafuente, J., Brackenridge, R.E., Juan, C., Stow, D.A. V, Sánchez-González, J.M., 2016. Oceanographic
738 processes and morphosedimentary products along the Iberian margins: A new multidisciplinary approach. *Mar*
739 *Geol* 378, 127–156. <http://dx.doi.org/10.1016/j.margeo.2015.12.008>
- 740 Holland, W.R., 1972. Baroclinic and topographic influences on the transport in western boundary currents. *Geophys*
741 *Fluid Dyn* 4, 187–210. <https://doi.org/10.1080/03091927208236095>
- 742 Iglesias, J., 2009. J. Sedimentation on the Cantabrian Continental Margin from Late Oligocene to Quaternary.
743 Universidade de Vigo, Ph.D. Thesis.
- 744 Iorga, M.C., Lozier, M.S., 1999a. Signatures of the Mediterranean outflow from a North Atlantic climatology 1. Salinity
745 and density fields. *J Geophys Res* 104, 25985–26009. <https://doi.org/10.1029/1999JC900115>
- 746 Iorga, M.C., Lozier, M.S., 1999b. Signatures of the Mediterranean outflow from a North Atlantic climatology 2.
747 Diagnostic velocity fields. *J Geophys Res* 104, 26011–26029. <https://doi.org/10.1029/1999JC900204>
- 748 Jackson, L., Hughes, C.W., Williams, R.G., 2006. Topographic Control of Basin and Channel Flows: The Role of Bottom
749 Pressure Torques and Friction. *J Phys Oceanogr* 36, 1786–1805. <https://doi.org/10.1175/JPO2936.1>
- 750 Juan, C., Ercilla, G., Javier Hernández-Molina, F., Estrada, F., Alonso, B., Casas, D., García, M., Farran, M., Llave, E.,
751 Palomino, D., Vázquez, J.-T., Medialdea, T., Gorini, C., D'Acromont, E., El Mounni, B., Ammar, A., 2016. Seismic
752 evidence of current-controlled sedimentation in the Alboran Sea during the Pliocene and Quaternary:
753 Palaeoceanographic implications. *Mar Geol* 378, 292–311. <http://dx.doi.org/10.1016/j.margeo.2016.01.006>
- 754 Kaboth, S., Bahr, A., Reichert, G.-J., Jacobs, B., Lourens, L.J., 2016. New insights into upper MOW variability over the last
755 150 kyr from IODP 339 Site U1386 in the Gulf of Cadiz. *Mar Geol* 377, 136–145.
756 <http://dx.doi.org/10.1016/j.margeo.2015.08.014>
- 757 Kaboth, S., de Boer, B., Bahr, A., Zeeden, C., Lourens, L.J., 2017. Mediterranean Outflow Water dynamics during the past
758 ~570 kyr: Regional and global implications. *Paleoceanography* 32, 634–647.
759 <https://doi.org/10.1002/2016PA003063>
- 760 Kvalstad, T.J., Andresen, L., Forsberg, C.F., Berg, K., Bryn, P., Wangen, M., 2005. The Storegga slide: evaluation of
761 triggering sources and slide mechanics. *Mar Pet Geol* 22, 245–256.
762 <https://doi.org/10.1016/j.marpetgeo.2004.10.019>
- 763 Laberg, J.S., Camerlenghi, A., 2008. Chapter 25 The Significance of Contourites for Submarine Slope Stability, in:
764 Rebesco, M., Camerlenghi, A. (Eds.), *Developments in Sedimentology*. Elsevier, pp. 537–556.
765 [http://dx.doi.org/10.1016/S0070-4571\(08\)10025-5](http://dx.doi.org/10.1016/S0070-4571(08)10025-5)
- 766 Laberg, J.S., Stoker, M.S., Dahlgren, K.I.T., Haas, H. de, Hafliðason, H., Hjelstuen, B.O., Nielsen, T., Shannon, P.M., Vorren,
767 T.O., van Weering, T.C.E., Ceramicola, S., 2005. Cenozoic alongslope processes and sedimentation on the NW
768 European Atlantic margin. *Mar Pet Geol* 22, 1069–1088. <http://dx.doi.org/10.1016/j.marpetgeo.2005.01.008>
- 769 Lamb, K.G., 2014. Internal Wave Breaking and Dissipation Mechanisms on the Continental Slope/Shelf. *Annu Rev Fluid*
770 *Mech* 46, 231–254. <https://doi.org/10.1146/annurev-fluid-011212-140701>
- 771 Lavín, A., Valdés, L., Sánchez, F., Abaunza, P., Forest, A., Boucher, J., Lazure, P., Jegou, A.M., 2006. The Bay of Biscay: the
772 countering of the ocean and the shelf, in: Brink, A.R.R.K.H. (Ed.), *The Sea. the President and Fellows of*
773 *Harvard College*, pp. 933–999.
- 774 Lazier, J.R.N., 1973. The renewal of Labrador sea water. *Deep Sea Res Oceanogr Abstr* 20, 341–353.
775 [http://dx.doi.org/10.1016/0011-7471\(73\)90058-2](http://dx.doi.org/10.1016/0011-7471(73)90058-2)
- 776 Lee, H.J., Syvitski, J.P.M., Parker, G., Orange, D., Locat, J., Hutton, E.W.H., Imran, J., 2002. Distinguishing sediment waves
777 from slope failure deposits: field examples, including the 'Humboldt slide', and modelling results. *Mar Geol* 192,
778 79–104. [http://dx.doi.org/10.1016/S0025-3227\(02\)00550-9](http://dx.doi.org/10.1016/S0025-3227(02)00550-9)
- 779 Llave, E., Hernandez-Molina, F.J., Somoza, L., Diaz-del Rio, V., Stow, D.A. V, Maestro, A., Alveirinho Dias, J.M., 2001.
780 Seismic stacking pattern of the Faro-Albufera contourite system (Gulf of Cadiz): a Quaternary record of
781 paleoceanographic and tectonic influences. *Mar Geophys Res* 22, 487–508.
782 <https://doi.org/10.1023/A:1016355801344>
- 783 Llave, E., Schönfeld, J., Hernandez-Molina, F.J., Mulder, T., Somoza, L., Diaz-del Rio, V., Sanchez-Almazo, I., 2006. High-
784 resolution stratigraphy of the Mediterranean outflow contourite system in the Gulf of Cadiz during the late

- 785 Pleistocene: The impact of Heinrich events. *Mar Geol* 277, 241–262.
786 <https://doi.org/10.1016/j.margeo.2005.11.015>
- 787 Locat, J., Lee, H.J., 2002. Submarine landslides: advances and challenges. *Can Geotech J* 39, 193–212.
788 <https://doi.org/10.1139/t01-089>
- 789 Maldonado, A., Barnolas, A., Bohoyo, F., Escutia, C., Galindo-Zaldívar, J., Hernández-Molina, J., Jabaloy, A., Lobo, F.J.,
790 Nelson, C.H., Rodríguez-Fernández, J., Somoza, L., Vázquez, J.-T., 2005. Miocene to Recent contourite drifts
791 development in the northern Weddell Sea. *Glob Planet Change* 45, 99–129.
792 <http://dx.doi.org/10.1016/j.gloplacha.2004.09.013>
- 793 Masson, D.G., Howe, J.A., Stoker, M.S., 2002. Bottom-current sediment waves, sediment drifts and contourites in the
794 northern Rockall Trough. *Mar Geol* 192, 215–237. [http://dx.doi.org/10.1016/S0025-3227\(02\)00556-X](http://dx.doi.org/10.1016/S0025-3227(02)00556-X)
- 795 McCartney, M.S., Mauritzen, C., 2001. On the origin of the warm inflow to the Nordic Seas. *Prog Oceanogr* 51, 125–214.
796 [http://dx.doi.org/10.1016/S0079-6611\(01\)00084-2](http://dx.doi.org/10.1016/S0079-6611(01)00084-2)
- 797 Mena, A., Francés, G., Pérez-Arlucea, M., Hanebuth, T.J.J., Bender, V.B., Nombela, M.A., 2018. Evolution of the Galicia
798 Interior Basin over the last 60 ka: sedimentary processes and palaeoceanographic implications. *J Quat Sci* 33,
799 536–549. <https://doi.org/doi:10.1002/jqs.3032>
- 800 Miramontes, E., Cattaneo, A., Jouet, G., Garziglia, S., 2016. Implications of Sediment Dynamics in Mass Transport along
801 the Pianosa Ridge (Northern Tyrrhenian Sea), in: Lamarche, G., Mountjoy, J., Bull, S., Hubble, T., Krastel, S., Lane,
802 E., Micallef, A., Moscardelli, L., Mueller, C., Pecher, I., Woelz, S. (Eds.), *Submarine Mass Movements and Their
803 Consequences: 7th International Symposium*. Springer International Publishing, Cham, 301–309.
804 https://doi.org/10.1007/978-3-319-20979-1_30 LB - Miramontes2016
- 805 Mosher, D.C., Thomson, R.E., 2002. The Foreslope Hills: large-scale, fine-grained sediment waves in the Strait of
806 Georgia, British Columbia. *Mar Geol* 192, 275–295. [http://dx.doi.org/10.1016/S0025-3227\(02\)00559-5](http://dx.doi.org/10.1016/S0025-3227(02)00559-5)
- 807 Muench, R.D., Wählin, A.K., Özgökmen, T.M., Hallberg, R., Padman, L., 2009. Impacts of bottom corrugations on a dense
808 Antarctic outflow: NW Ross Sea. *Geophys Res Lett* 36. <https://doi.org/doi:10.1029/2009GL041347>
- 809 Muñoz, J.A., 2002. The Pyrenees. *The Geology of Spain*, The Geological Society, London (2002), 370–385.
- 810 Cadenas, P., Fernandez-Viejo, G., 2016. The Asturian Basin within the North Iberian margin (Bay of Biscay): seismic
811 characterisation of its geometry and its Mesozoic and Cenozoic cover. *Basin Res* 29, 521–541.
812 <https://doi.org/doi:10.1111/bre.12187>
- 813 Palomino, D., López-González, N., Vázquez, J.-T., Fernández-Salas, L.-M., Rueda, J.-L., Sánchez-Leal, R., Díaz-del-Río, V.,
814 2016. Multidisciplinary study of mud volcanoes and diapirs and their relationship to seepages and bottom
815 currents in the Gulf of Cádiz continental slope (northeastern sector). *Mar Geol* 378, 196–212.
816 <https://doi.org/10.1016/j.margeo.2015.10.001>
- 817 Pingree, R.D., 1993. Flow of surface waters to the west of the British Isles and in the Bay of Biscay. *Deep Sea Res Part II*
818 *Top Stud Oceanogr* 40, 369–388. [http://dx.doi.org/10.1016/0967-0645\(93\)90022-F](http://dx.doi.org/10.1016/0967-0645(93)90022-F)
- 819 Pingree, R.D., Le Cann, B., 1992. Three anticyclonic slope water oceanic eDDIES (SWODDIES) in the Southern Bay of
820 Biscay in 1990. *Deep Sea Res Part A Oceanogr Res Pap* 39, 1147–1175. [http://dx.doi.org/10.1016/0198-0149\(92\)90062-X](http://dx.doi.org/10.1016/0198-0149(92)90062-X)
- 822 Pingree, R.D., Le Cann, B., 1990. Structure, strength and seasonality of the slope currents in the Bay of Biscay region. *J*
823 *Mar Biol Assoc United Kingdom* 70, 857–885. <https://doi.org/10.1017/S0025315400059117>
- 824 Pollard, R.T., Griffthts, M.J., Cunningham, S.A., Read, J.F., Pérez, F.F., Ríos, A.F., 1996. Vivaldi 1991 - A study of the
825 formation, circulation and ventilation of Eastern North Atlantic Central Water. *Prog Oceanogr* 37, 167–192.
826 [http://dx.doi.org/10.1016/S0079-6611\(96\)00008-0](http://dx.doi.org/10.1016/S0079-6611(96)00008-0)
- 827 Pomar, L., Morsilli, M., Hallock, P., Bádenas, B., 2012. Internal waves, an under-explored source of turbulence events in
828 the sedimentary record. *Earth-Science Rev* 111, 56–81. <http://dx.doi.org/10.1016/j.earscirev.2011.12.005>
- 829 Prego, R., Boi, P., Cobelo-García, A., 2008. The contribution of total suspended solids to the Bay of Biscay by Cantabrian
830 Rivers (northern coast of the Iberian Peninsula) Bay of Biscay. *J Mar Syst* 72, 342–349.
831 <http://dx.doi.org/10.1016/j.jmarsys.2007.01.011>
- 832 Preu, B., Hernández-Molina, F.J., Violante, R., Piola, A.R., Paterlini, C.M., Schwenk, T., Voigt, I., Krastel, S., Spiess, V., 2013.
833 Morphosedimentary and hydrographic features of the northern Argentine margin: The interplay between
834 erosive, depositional and gravitational processes and its conceptual implications. *Deep Sea Res Part I Oceanogr*
835 *Res Pap* 75, 157–174. <http://dx.doi.org/10.1016/j.dsr.2012.12.013>

- 836 Preu, B., Schwenk, T., Hernández-Molina, F.J., Violante, R., Paterlini, M., Krastel, S., Tomasini, J., Spieß, V., 2012.
837 Sedimentary growth pattern on the northern Argentine slope: The impact of North Atlantic Deep Water on
838 southern hemisphere slope architecture. *Mar Geol* 329–331, 113–125.
839 <https://doi.org/10.1016/j.margeo.2012.09.009>
- 840 Rashid, H., MacKillop, K., Sherwin, J., Piper, D.J.W., Marche, B., Vermooten, M., 2017. Slope instability on a shallow
841 contourite-dominated continental margin, southeastern Grand Banks, eastern Canada. *Mar Geol* 393, 203–215.
842 <https://doi.org/10.1016/j.margeo.2017.01.001>
- 843 Rebesco, M., Camerlenghi, A., Van Loon, A.J., 2008. Chapter 1 Contourite Research: A Field in Full Development, in:
844 Rebesco, M., Camerlenghi, A. (Eds.), *Developments in Sedimentology*. Elsevier, pp. 1–10.
845 [http://dx.doi.org/10.1016/S0070-4571\(08\)10001-2](http://dx.doi.org/10.1016/S0070-4571(08)10001-2)
- 846 Rebesco, M., Hernández-Molina, F.J., Van Rooij, D., Wählin, A., 2014. Contourites and associated sediments controlled
847 by deep-water circulation processes: State-of-the-art and future considerations. *Mar Geol* 352, 111–154.
848 <http://dx.doi.org/10.1016/j.margeo.2014.03.011>
- 849 Ribó, M., Puig, P., Muñoz, A., Lo Iacono, C., Masqué, P., Palanques, A., Acosta, J., Guillén, J., Gómez Ballesteros, M., 2016.
850 Morphobathymetric analysis of the large fine-grained sediment waves over the Gulf of Valencia continental
851 slope (NW Mediterranean). *Geomorphology* 253, 22–37. <http://dx.doi.org/10.1016/j.geomorph.2015.09.027>
- 852 Ríos, A.F., Pérez, F.F., Fraga, F., 1992. Water masses in the upper and middle North Atlantic Ocean east of the Azores.
853 *Deep Sea Res Part A Oceanogr Res Pap* 39, 645–658. [http://dx.doi.org/10.1016/0198-0149\(92\)90093-9](http://dx.doi.org/10.1016/0198-0149(92)90093-9)
- 854 Roca, E., Muñoz, J.A., Ferrer, O., Ellouz, N., 2011. The role of the Bay of Biscay Mesozoic extensional structure in the
855 configuration of the Pyrenean orogen: Constraints from the MARCONI deep seismic reflection survey. *Tectonics*
856 30, TC2001. <https://doi.org/10.1029/2010TC002735>
- 857 Rogerson, M., Rohling, E.J., Bigg, G.R., Ramirez, J., 2012. Paleooceanography of the Atlantic-Mediterranean exchange:
858 Overview and first quantitative assessment of climatic forcing. *Rev Geophys* 50, RG2003.
859 <https://doi.org/10.1029/2011RG000376>
- 860 Rumín-Caparrós, A., Sanchez-Vidal, A., Calafat, A., Canals, M., Martín, J., Puig, P., Pedrosa-Pàmies, R., 2013. External
861 forcings, oceanographic processes and particle flux dynamics in Cap de Creus submarine canyon, NW
862 Mediterranean Sea. *Biogeosciences* 10, 3493–3505. <https://doi.org/10.5194/bg-10-3493-2013>
- 863 Rumín-Caparrós, A., Sanchez-Vidal, A., González-Pola, C., Lastras, G., Calafat, A., Canals, M., 2016. Particle fluxes and
864 their drivers in the Avilés submarine canyon and adjacent slope, central Cantabrian margin, Bay of Biscay. *Prog*
865 *Oceanogr* 144, 39–61. <http://dx.doi.org/10.1016/j.pocean.2016.03.004>
- 866 Shanmugam, G., 2013. New perspectives on deep-water sandstones: Implications. *Pet Explor Dev* 40, 316–324.
867 [http://dx.doi.org/10.1016/S1876-3804\(13\)60038-5](http://dx.doi.org/10.1016/S1876-3804(13)60038-5)
- 868 Speer, K.G., Gould, J., LaCasce, J., 1999. Year-long float trajectories in the Labrador Sea Water of the eastern North
869 Atlantic Ocean. *Deep Sea Res Part II Top Stud Oceanogr* 46, 165–179. [https://doi.org/10.1016/S0967-0645\(98\)00103-9](https://doi.org/10.1016/S0967-0645(98)00103-9)
870
- 871 Stoker, M.S., Houlst, R.J., Nielsen, T., Hjelstuen, B.O., Laberg, J.S., Shannon, P.M., Praeg, D., Mathiesen, A., van Weering,
872 T.C.E., McDonnell, A., 2005. Sedimentary and oceanographic responses to early Neogene compression on the
873 NW European margin. *Mar Pet Geol* 22, 1031–1044. <https://doi.org/10.1016/j.marpetgeo.2005.01.009>
- 874 Stow, D.A.V., Faugères, J.-C., Howe, J.A., Pudsey, C.J., Viana, A.R., 2002. Bottom currents, contourites and deep-sea
875 sediment drifts: current state-of-the-art. *Geol Soc London, Mem* 22, 7–20.
876 <https://doi.org/10.1144/gsl.mem.2002.022.01.02>
- 877 Stow, D.A.V., Hernández-Molina, F.J., Llave, E., Bruno, M., García, M., Díaz del Río, V., Somoza, L., Brackenridge, R.E.,
878 2013. The Cadiz Contourite Channel: Sandy contourites, bedforms and dynamic current interaction. *Mar Geol*
879 343, 99–114. <http://dx.doi.org/10.1016/j.margeo.2013.06.013>
- 880 Stow, D.A.V., Hunter, S., Wilkinson, D., Hernández-Molina, F.J., 2008. Chapter 9 The Nature of Contourite Deposition, in:
881 Rebesco, M., Camerlenghi, A. (Eds.), *Developments in Sedimentology*. Elsevier, pp. 143–156.
882 [http://dx.doi.org/10.1016/S0070-4571\(08\)10009-7](http://dx.doi.org/10.1016/S0070-4571(08)10009-7)
- 883 Stow, D.A.V., Javier Hernández-Molina, F., Llave, E., Sayago, M., 2009. Bedform-velocity matrix: The estimation of
884 bottom current velocity from bedform observations. *Geology* 37, 327–330. <https://doi.org/10.1130/G25259A.1>
- 885 Sultan, N., Cochonot, P., Canals, M., Cattaneo, A., Dennielou, B., Haflidason, H., Laberg, J.S., Long, D., Mienert, J., Trincardi,
886 F., Urgeles, R., Vorren, T.O., Wilson, C., 2004. Triggering mechanisms of slope instability processes and sediment
887 failures on continental margins: a geotechnical approach. *Mar Geol* 213, 291–321.
888 <https://doi.org/10.1016/j.margeo.2004.10.011>

- 889 Tournadour, E., Mulder, T., Borgomano, J., Hanquiez, V., Ducassou, E., Gillet, H., 2015. Origin and architecture of a Mass
890 Transport Complex on the northwest slope of Little Bahama Bank (Bahamas): Relations between off-bank
891 transport, bottom current sedimentation and submarine landslides. *Sedimentary Geology*, 317, 9–26.
892 <http://dx.doi.org/10.1016/j.sedgeo.2014.10.003>
- 893 Tugend, J., Manatschal, G., Kuszniir, N.J., Masini, E., Mohn, G., Thimon, I., 2014. Formation and deformation of
894 hyperextended rift systems: Insights from rift domain mapping in the Bay of Biscay-Pyrenees. *Tectonics* 33,
895 1239–1276. <https://doi.org/10.1002/2014TC003529>
- 896 Turnewitsch, R., Reyss, J.L., Chapman, D.C., Thomson, J., Lampitt, R.S., 2004. Evidence for a sedimentary fingerprint of
897 an asymmetric flow field surrounding a short seamount. *Earth Planet Sci Lett* 222, 1023–1036.
898 <https://doi.org/10.1016/j.epsl.2004.03.042>
- 899 van Aken, H.M., 2000a. The hydrography of the mid-latitude northeast Atlantic Ocean: I: The deep water masses. *Deep*
900 *Sea Res Part I Oceanogr Res Pap* 47, 757–788. [http://dx.doi.org/10.1016/S0967-0637\(99\)00092-8](http://dx.doi.org/10.1016/S0967-0637(99)00092-8)
- 901 van Aken, H.M., 2000b. The hydrography of the mid-latitude Northeast Atlantic Ocean: II: The intermediate water
902 masses. *Deep Sea Res Part I Oceanogr Res Pap* 47, 789–824. [http://dx.doi.org/10.1016/S0967-0637\(99\)00112-](http://dx.doi.org/10.1016/S0967-0637(99)00112-0)
903 0
- 904 Van Rooij, D., Blamart, D., Kozachenko, M., Henriot, J.-P., 2007. Small mounded contourite drifts associated with deep-
905 water coral banks, Porcupine Seabight, NE Atlantic Ocean. *Geol Soc London, Spec Publ* 276, 225–244.
906 <https://doi.org/10.1144/gsl.sp.2007.276.01.11>
- 907 Van Rooij, D., Campbell, C., Rueggeberg, A., Wahlin, A., 2016. The contourite log-book: significance for
908 palaeoceanography, ecosystems and slope instability. *Mar Geol* 378, 1–4.
909 <http://dx.doi.org/10.1016/j.margeo.2016.05.018>
- 910 Van Rooij, D., Iglesias, J., Hernández-Molina, F.J., Ercilla, G., Gomez-Ballesteros, M., Casas, D., Llave, E., De Hauwere, A.,
911 Garcia-Gil, S., Acosta, J., Henriot, J.P., 2010. The Le Danois Contourite Depositional System: Interactions between
912 the Mediterranean Outflow Water and the upper Cantabrian slope (North Iberian margin)(Bay of Biscay). *Mar*
913 *Geol* 274, 1–20. <http://dx.doi.org/10.1016/j.margeo.2010.03.001>
- 914 Vandorpe, T., Martins, I., Vitorino, J., Hebbeln, D., García, M., Van Rooij, D., 2016. Bottom currents and their influence on
915 the sedimentation pattern in the El Arraiche mud volcano province, southern Gulf of Cadiz. *Mar Geol* 378, 114–
916 126. <https://doi.org/10.1016/j.margeo.2015.11.012>
- 917 Verdicchio, G., Trincardi, F., 2008. Chapter 20 Shallow-Water Contourites, in: Rebesco, M., Camerlenghi, A. (Eds.),
918 *Developments in Sedimentology*. Elsevier, pp. 409–433. [http://dx.doi.org/10.1016/S0070-4571\(08\)10020-6](http://dx.doi.org/10.1016/S0070-4571(08)10020-6)
- 919 Vergés, J., Fernández, M., Martínez, A., 2002. The Pyrenean orogen: pre-, syn-, and post-collisional evolution. G.
920 Rosenbaum, G.S. Lister (Eds.), *Reconstruction of the evolution of the Alpine–Himalayan Orogen*, *J Virtual Explor*
921 8, 55–74.
- 922 Vissers, R.L.M., Meijer, P.T., 2012. Iberian plate kinematics and Alpine collision in the Pyrenees. *Earth-Science Rev* 114,
923 61–83. <https://doi.org/10.1016/j.earscirev.2012.05.001>
- 924 von Lom-Keil, H., Spieß, V., Hopfauf, V., 2002. Fine-grained sediment waves on the western flank of the Zapiola Drift,
925 Argentine Basin: evidence for variations in Late Quaternary bottom flow activity. *Mar Geol* 192, 239–258.
926 [http://dx.doi.org/10.1016/S0025-3227\(02\)00557-1](http://dx.doi.org/10.1016/S0025-3227(02)00557-1)
- 927 Weigelt, E., Uenzelmann-Neben, G., 2004. Sediment deposits in the Cape Basin: Indications for shifting ocean currents?
928 *Am Assoc Pet Geol Bull* 88, 765–780. <http://dx.doi.org/10.1306/01260403101>
- 929 Wilson, C.K., Long, D., Bulat, J., 2004. The morphology, setting and processes of the Afen Slide. *Mar Geol* 213, 149–167.
930 <https://doi.org/10.1016/j.margeo.2004.10.005>
- 931 Wynn, R.B., Masson, D.G., 2008. Chapter 15 Sediment Waves and Bedforms, in: Rebesco, M., Camerlenghi, A. (Eds.),
932 *Developments in Sedimentology*. Elsevier, pp. 289–300. [http://dx.doi.org/10.1016/S0070-4571\(08\)10015-2](http://dx.doi.org/10.1016/S0070-4571(08)10015-2)
- 933 Wynn, R.B., Stow, D.A. V, 2002. Classification and characterisation of deep-water sediment waves. *Mar Geol* 192, 7–22.
934 [http://dx.doi.org/10.1016/S0025-3227\(02\)00547-9](http://dx.doi.org/10.1016/S0025-3227(02)00547-9)
- 935 Zhang, W., Hanebuth, T.J.J., Stöber, U., 2016. Short-term sediment dynamics on a meso-scale contourite drift (off NW
936 Iberia): Impacts of multi-scale oceanographic processes deduced from the analysis of mooring data and
937 numerical modelling. *Mar Geol* 378, 81–100. <http://dx.doi.org/10.1016/j.margeo.2015.12.006>

938

939 **Figures**

940 **Fig. 1.** Location of the study area: A) Position with respect to the North Iberian continental margin (Ercilla
941 et al., 2008), contour lines every 500 m. Location of the rivers is based on Prego et al. (2008); B) Available
942 geophysical datasets for this study. The present-day oceanographic circulation pattern is modified from
943 González-Pola et al. (2012). The main morphological expressions are shown (contour lines every 100 m).
944 ENACW = Eastern North Atlantic Central Water; AMW = Atlantic Mediterranean Water; LSW = Labrador
945 Sea Water.

946 **Fig. 2.** Multibeam bathymetry map of the study area, with the location of displayed seismic profiles.

947 **Fig. 3.** Slope map (in degrees) of the study area. The identified contourite deposits (outlined in red) and
948 slide scars are indicated.

949 **Fig. 4.** (a) 3D colour shaded relief multibeam high-resolution bathymetric map of the study area
950 (ECOMARG project, IEO), with the location of oceanographic cross-sections A-A', B-B' and C-C (World
951 Ocean Database, 2013). (b) Potential temperature versus salinity diagram from the water masses in the
952 study area (World Ocean Database, 2013). CTD stations (red triangles) and their respective locations are
953 indicated in cross-section profiles (c, d, e, f). Oceanographic cross-sections from the Le Danois Bank
954 towards the Cantabrian continental margin. The water column colour ranges indicate salinity (c, e, f) and
955 temperature (d).

956 **Fig. 5.** Morphosedimentary map of the Le Danois Bank region, based on the interpretation of multibeam
957 bathymetry and seismic profiles. Numbers (1-6) and letters (A, B, C) respectively denote plastered drifts
958 and sediment wave fields.

959 **Fig. 6.** Interpreted sparker seismic profiles showing the morphological features of elongated mounded
960 and separated drifts and a plastered drift. Onlap and downlap terminations (red arrows) are indicated.
961 The location the seismic lines is indicated on the multibeam bathymetry map (Fig. 2).

962 **Fig. 7.** Interpreted sparker (a, b), TOPAS (c, d) and airgun (e) seismic profiles showing the morphological
963 features of plastered drifts and slide scars. Onlap and downlap terminations (red arrows) are indicated.
964 The location of the seismic lines is indicated on the multibeam bathymetry map (Fig. 2).

965 **Fig. 8.** Interpreted sparker (a, b, d, e) and airgun (c, f) seismic profiles showing the morphological features
966 of slide scars, mass-transport deposits and sediment waves. The location of the seismic lines is indicated
967 on the multibeam bathymetry map (Fig. 2).

968 **Fig. 9.** Seismic and oceanographic profiles in the Le Danois Bank region. The depth intervals of the water
969 masses and contourite features show the dynamic interaction between water masses and the present-day
970 sedimentary regime. The locations of airgun seismic profiles are indicated in the bathymetric map. The
971 junctions of Line a, b and f; and Line e and g (dotted black lines) are indicated in the seismic profiles. The
972 CTD stations (red triangles) and their respective locations are indicated in the seismic and oceanographic
973 profiles.

974 **Fig. 10.** Sketch of the recent sedimentary processes within the Le Danois Bank region. This sketch has
975 been produced based on the morphosedimentary features defined in the morphosedimentary map (Fig. 5).

976

Highlights:

- Present-day morphology of the Le Danois Bank region is shaped by alongslope, downslope and mixed processes.
- Due to the morphological constraint of the Le Danois Bank and the Vizco High, bottom currents are more focused and strongly intensified (estimated acceleration up to 25 cm/s).
- Contourite drifts are suggested to have specific geometries and shapes in topographically constrained small basins.
- More frequent lateral variations are typical features for contourite drifts generating in topographically constrained small basins.